The Pennsylvania State University

The Graduate School

FLOWING ELECTROLYTE METAL BATTERIES

A Dissertation in

Mechanical Engineering

by

Mihir Parekh

Submitted in Partial Fulfillment
of the Requirements
for the Degree of

Doctor of Philosophy

December 2021

The dissertation of Mihir Parekh was reviewed and approved by the following:

Christopher D. Rahn
J. 'Lee' Everett Professor and Associate Dean for Innovation
Dissertation Advisor
Chair of Committee

Chao-Yang Wang
Professor and Diefenderfer Chair

Sukwon Choi
Kenneth Kuan-Yun Kuo Early Career Professor

Long-Qing Chen
Hamer Professor of Materials Science and Engineering, Professor of Engineering Science and Mechanics, Professor of Mathematics

Daniel Haworth
Professor of Mechanical Engineering
Associate Head for Graduate Programs in Mechanical Engineering

Abstract

Instabilities during metal electrodeposition create dendrites on the plating surfaces. In high energy density lithium metal batteries (LMBs) dendrite growth causes safety issues and accelerated aging. In this thesis, analytical models predict that dendrite growth can be controlled and potentially eliminated by small advective flows normal to the surface of lithium metal electrode introducing a new class of batteries, namely, flowing electrolyte metal batteries (FEMBs). Electrolyte flow towards the Li metal electrode lowers the dendrite growth rate, overpotential, and impedance. Flow in the opposite direction, however, enhances the dendrite growth. For every current density, there exists a velocity above which dendrite growth can be totally eliminated. The critical velocity increases almost linearly with increasing current density. For typical current densities and inter-electrode separation, the critical velocity is of the order of $\mu m/s$, indicating the potential for practical application. The critical flow velocity scales linearly with charging rate, requiring 37 mL/Ah of flow volume.

The effect of creeping electrolyte flow through perforated metal anodes on dendrite growth and energy density is further analyzed using a 2D COMSOL Multiphysics model. The flowing electrolyte enhances plating inside the slot (2D model of pore) and reduces plating on the part of electrode directly facing the counter-electrode. This reduces the chances of short circuit via dendrite growth. Larger slot separation, lower slot widths, and thicker electrodes alleviate dendrite growth but lower the specific charge density. Very narrow slots may get plugged due to plating inside the hole. Thus, slot width, slot separation, and electrode thickness should be optimized to ensure high specific charge density and non-dendritic plating in the inter-slot gap.

We also derive analytical models for electrodeposition with creeping Poiseuille and Couette flows parallel to the two electrodes. The models predict that creeping electrolyte flow parallel to the surface of metal electrode increases the stability of lithium plating by reducing the dendrite growth rate. Moreover, parallel flow reduces the curvature of dendrites leading to flatter electrodeposits. For the same average flow rate, Poiseuille flow can be upto two times more stabilizing than Couette flow. It is also not possible to completely stabilize the metal electrode with creeping parallel flows.

In LMBs, solid electrolyte interphase (SEI) growth reduces coulombic efficiency and cycle life. In this thesis, we develop a steady-state model that predicts that small advective electrolyte flow towards the lithium metal electrode at a fixed current density

improves the coulombic efficiency and decreases SEI layer growth rate. Low flow rates ($\mu m/s$) can increase coulombic efficiency by up to 6%, extending capacity retention and cycle life by a factor of 7X. The sensitivity of the coulombic efficiency to plating and SEI layer reaction rate constant is also explored. Higher plating reaction rate constant and lower SEI formation rate constant leads to higher coulombic efficiency.

Zinc metal batteries are a widely considered alternative to lithium metal batteries that also suffer from dendrite growth. We explore the effect of creeping normal electrolyte flow on dendrite growth in zinc metal batteries using a transient model that predicts concentration distribution evolution and a linear stability analysis that predicts dendrite growth. Dendrite growth on zinc metal anodes can occur due to surface instabilities and/or concentration depletion. Creeping normal flow with a flow rate greater than the critical flow rate ensures stable plating and prevents ion depletion near the negative electrode, thus eliminating both causes of dendrite growth. Unlike lithium, increasing the flow rate does not necessarily reduce the electrostatic potential difference between the two electrodes, thus indicating the importance of ion diffusivity ratio in the electrolyte impedance.

Table of Contents

List of Figures

List of Tables

Acknowledgements

I thank my advisor Dr. Christopher Rahn for constantly guiding me through the course of this project. Our discussions with our collaborators, Dr. Lynden Archer and Dr. Donald Koch have been very helpful to us. So, I wish to thank both of them as well. I am also indebted to my committee members Dr. Chao-Yang Wang, Dr. Sukwon Choi and Dr. Long-Qing Chen as their thoughtful comments during my comprehensive exam have helped me refine my thesis. I would also like to thank Dr. Anil Kulkarni, who mentored me during my role as a teaching assistant for his course in Fall 2018. This material is based upon work supported by the National Science Foundation under Award No. 1662055. Any opinions, findings, and conclusions or recommendations expressed in this material are those of the author and do not necessarily reflect views of the National Science Foundation.

Although experimental results have not been included in the thesis, I have built the experimental setup to test our model and my lab-mate Shuhua Shan has taken over the experimental work from me. Dr. Rong Kou's help and collaboration with us for the experimental work is highly appreciated. Dr. Donghai Wang has very generously allowed us to utilize his lab space and lab equipments for our experiments and so I am very thankful to him. I am very grateful to Timothy Cleary who has helped me use the ARBIN machine to plate electrodes for my experiments.

I wish to express my heartfelt gratitude to my other lab mates George Rai, Valentin Laneri, Kiran Bhaskar, Changik Cho, Dr. Jun Ma, Dr. Tahzib Safwat, Michael Trowbridge, Matthew Lenko, and Dr. Matthew Krott for their constant moral support. Finally, I express my gratitude towards my parents (Mr. Narayan Parekh and Mrs. Vandana Parekh) and grandparents (Mr. Shivshankar Parekh and Mrs. Narmada Parekh) as it is their constant encouragement that has kept me sane through my arduous PhD journey.

Chapter 1
Introduction

Metals such as lithium, sodium, magnesium, and zinc are increasingly being investigated as potential anodes for rechargeable batteries. Lithium metal batteries (LMBs) in particular, with high theoretical volumetric and gravimetric energy densities, are amongst the highest performing cells [1]. However, electroplating on the lithium metal electrode surface during charging often leads to dendrite growth. Moreover, Li, due to its high reactivity, also reacts with the electrolyte to produce a Solid Electrolyte Interphase (SEI). The coupling of dendrite growth and SEI formation on Li metal electrodes often leads to SEI cracking. This compounds the problem by producing dead Li that contributes to low coulombic efficiency and short cycle life. SEI cracking also promotes dendrite growth which can also lead to internal shorting with potential fires and explosions [2].

1.1 Dendrite growth in LMBs

There are many models in literature which investigate dendrite growth. Chazelviel's work [3] throws light upon the role of mass transport limitations and ion depletion at dendrite tips in governing dendrite growth. Ion depletion occurs due to concentration gradient and concentration of electric field lines at the dendrite tips. Nishikawa *et al.* [4], perform experiments to investigate the importance of mass transfer effects in dendrite

growth. Dendrite growth due to ion depletion should occur only at current densities above limiting current densities and after Sand's time [5]. However, dendrite growth on lithium metal electrode has been observed at much lower current densities and before Sand's time [6–8]. This shows that local effects often govern dendrite growth. After initial plating which leads to mossy Li growth, electrolyte near the inhomogeneously plated surface created by plating gets confined. After electrolyte confinement, local concentration gradients govern the plating mechanism and local ion depletion can lead to dendrite growth even when bulk charging current density is less than the limiting charging current density [9]. Wood *et al.* [10], for the first time, perform in-situ video operando microscopy for galvanostatic electrodeposition in Li|Li symmetric cells and relate the different parts of the obtained voltage trace to various processes happening during electrodepostion. Electrodepostion first happens on dendrite tips and then on pits in the pristine Li surfaces. During discharge, stripping also takes place preferentially at dendrite tips. However, stress related fracture at the roots can create dead Li and hence all the plated Li on the tips does not remain electrochemically active. This leads to stripping from fresh Li surfaces which creates pits. Ely *et al.* [11] identify five regimes of dendrite growth, namely, nucleation suppression regime, long incubation time regime, short incubation time regime, early growth regime, and late growth regime. The transition from one regime to another depends on a thermodynamically determined critical overpotential, and a critical radius governed by kinetics. Akolkar derives an expression for dendrite growth rate under pure activation control [12]. Jana *et al.* [8] couple the stress driven and transport limitation driven dendrite growth models and identify various regimes of dendrite growth. Yan *et al.* [13] study the effect of temperature gradients on dendrite morphology. Using, the Arrhenius temperature dependent model [14], Akolkar identified a current density dependent critical temperature below which uncontrolled dendrite growth maybe initiated. None of these models, however, predict the stability

of the electrodeposition process. Sundstrom *et al.* [15] and Tikekar *et al.* [16] perform stability analysis for the electrodeposition process and show that surface tension and electrode curvature are two important factors governing dendrite growth. They show the presence of a maxima in the curve of dendrite growth rate versus wavenumber and also show that stable electroplating may be obtained above a critical wavenumber. The presence of a critical wavenumber throws light upon the importance of electrode geometry in controlling dendrite growth. Through their transient linear stability analysis, Khoo *et al.* [17] show that dendrite growth can be controlled by surface conduction in charged nanopores. The results that they obtain from linear stability analysis match well with the experimental results obtained from copper electrodeposition, thus confirming the validity of this technique. Elezgaray *et al.* [18] identify two distinct unstable electroplating regimes through their transient stability analysis of unsteady galvanostatic electrodepostion in 2D diffusion limited regime. Gireaud *et al.* [19] demonstrates the role of internal pressure in governing dendrite growth. Pulsed electrodeposition is another potential method to control dendrite growth [20–22].

Maraschky *et al.* [23] show that increasing thickness of SEI layer which leads to ion depletion at the electrode surface is the main cause of dendrite growth. Dead Li formed by an unstable SEI leads to a decrease in coulombic efficiency and capacity [24]. Maraschky *et al.* extend their work and further explore the effect of temperature on transport through SEI layer [25] as it is tied to dendrite growth. Unstable SEI layers may lead to the production of dead Li and decreased coulombic efficiency and capacity [24]. Unstable SEI layer can also lead to dendrite growth. So, stabilizing the SEI is another method to control dendrite growth. A variety of electrolyte additives [26–29] and protective layers on the lithium metal electrode [30, 31] have been shown to stabilize the SEI. Uniform metal ion flux [32, 33] reduces the concentration gradients at dendrite tips and

suppresses dendrite growth. Using 3D porous structured anodes with large number of polar groups [34] or a 3D mixed ion-electron conductors (MIEC) [35] can potentially suppress dendrites. Homogeneous Li nucleation on polymer brushes with lithiophilic functional groups [36] and homogeneous, localized or gradient distributed lithium ion flux [37] can potentially eliminate dendrites. Bai *et al.* [38] demonstrate that sharp dendrites that grow at current densities higher than bulk limiting current density can penetrate through nanoporous ceramic separators. However, nanoporous ceramic separators can successfully stop root-growing mossy lithium at current densities below bulk limiting current density [39]. Rehnlund *et al.* [40] stress upon the importance on electrolyte concentration in controlling dendrite growth.

Techniques such as magnetic stirring of electrolyte [41], Lorentz force (j x B, where B is the magnetic field) [42], electrokinetic pumping through a sponge like structure [43] may eliminate dendrite growth in some situations by enhancing mass transport. However, since Lorentz force is primarily normal to the primary ion flux high magnetic field or large electrode curvatures maybe required to achieve dendrite free plating. Replenishment of electrolyte near dendrite tips by vortex formation can alter the dendrite morphology from straight to mossy [44].

1.2 SEI layer growth in LMBs

Solid electrolyte interphase (SEI) growth is another important feature of Li metal batteries. Due to their high reactivity, lithium metal electrodes often react instantaneously with the electrolyte to form SEI [45]. Stripping Li from under the SEI during discharging can lead to the formation of nanovoids. Aggregation of nanovoids at high discharge rates can lead to the collapse of the SEI layer (pitting), exposing fresh Li surfaces and consuming further Li [46] in SEI generation. These inhomogeneities in the Li metal

surface formed due to repeated stripping and pitting produce surface irregularities that promote dendrite growth. Discharging at high current can lead to rapid SEI growth and increased impedance, thus making fast charging difficult. Lu *et al.* [47] suggest this mechanism as the root cause of failure in Li metal batteries. A mechanically tough SEI may withstand stress, reduce dendrite growth, and prevent consumption of Li during repeated cycling as fresh Li surfaces are not exposed to the electrolyte if the SEI layer does not break [48]. SEI layer growth has been studied extensively in theoretical, computational, first-principles modeling, and experimental studies [49].

Modeling plays a key role in understanding the SEI growth mechanism. The model based on electron-tunneling proposed by Peled [45] is one of the pioneering works in this field. Broussley *et al.* [50] propose a growth model limited by electronic conductivity of the SEI layer and link SEI layer growth to capacity degradation and aging in Li ion batteries. Ploehn *et al.* [51] propose a growth mechanism dominated by solvent diffusion through the SEI layer. Christensen *et al.* [52] derive a mathematical model for SEI layer growth and investigate the dependence of SEI layer growth on battery voltage. They argue that the characteristics and chemical composition of SEI layers on lithium and graphite electrodes are similar. Pinson *et al.* [53] derive the square root dependence of long term SEI layer growth on time using single particle and porous electrode models and a solvent diffusion limited growth mechanism. The long term square root dependence may also be derived by using growth mechanisms associated with electronic conduction or neutral lithium interstitial diffusion through the SEI layer [54]. A linear dependence of SEI growth with time results from linearization of the single particle model and SEI growth rate kinetics [55]. Single *et al.* [54] show that a growth mechanism limited by diffusion of lithium interstitials through the SEI can reproduce the potential dependence of long term SEI growth. With increasing SEI porosity, the SEI growth mechanism tran-

sitions from electronic conduction limited growth to solvent diffusion limited growth. Attia *et al.* [56] experimentally show that even within the same charge-discharge cycle the SEI layer growth is faster while charging than during discharging. Das *et al.* [57] build a theoretical model based on a mixed ionic electronic conductor SEI to explain these experimental results.

Kim *et al.* [58] study the effect of electrolyte composition on structure and evolution of SEI via molecular dynamics simulations. Bertolini *et al.* [59] use reactive molecular dynamics simulations to study the initial stages of formation of SEI on Li metal electrodes in the absence of a bias potential. They identify a porous phase in contact with the Li metal electrode, a nest phase, and a disperse phase in the SEI and propose that uneven Li distribution in the nest phase may be responsible for uneven electric field and dendrite growth.

The SEI layer often contains both organic and inorganic products [48,60] and its composition depends upon electrolyte composition [61,62], temperature [63] and charge-discharge current [64]. A stable SEI is thought to prevent dendrite growth, so researchers use SEI forming additives in the electrolyte [26,65–67] and grow artificial SEI layers in-situ [68,69] and ex-situ [70–72]. Indirect strategies to stabilize the SEI include changing electrolyte concentration [73, 74] and modifying the host [75, 76] and separator [77, 78] materials. Reported coulombic efficiencies range from 92% [79] to 99.1% [71].

1.3 Flowing electrolyte metal batteries

This thesis shows that flowing electrolyte metal batteries (FEMBs) has demonstrate dendrite suppression theoretically with corroborating experiments in [80]. In chapters 2 and 3, we show that creeping flow normal to the lithium metal electrode and above a critical

speed can theoretically eliminate dendrite growth. Chapter 4 shows that creeping flow parallel to the lithium metal electrode can also reduce dendrite growth. Dendrite and SEI layer growth in LMBs are inherently coupled. Chapter 5 develops the first steady-state model of a lithium metal electrode with normal electrolyte flow including ion and solvent diffusion and SEI layer growth kinetics. The model predicts the current distribution between plating and SEI layer growth and also identifies the reaction parameters that may be required to achieve high coulombic efficiencies.

1.4 Zinc metal batteries

Zinc batteries are receiving attention because Zn is an easily available and inexpensive metal, making Zn batteries a low cost option. Low cycle life [81] associated with irreversible electrochemistry above a certain depth of discharge [82] has prevented commercialization of rechargeable Zn batteries. Moreover, the morphology change of Zn metal [83] with cycling leads to the formation of dead Zn reducing the battery capacity and lifetime. Zn also has a high modulus compared to Li, so Zn dendrites can easily penetrate the separator leading to internal short circuits [84–87]. Zinc deposits have different morphologies which depend upon the ratio of charging current density to limiting current density. For underlimiting conditions, the zinc plates are oriented in the electrode plane. They grow perpendicular to the electrode plane, however, they tilt in overlimiting conditions [88]. For dilute electrolytes, various diffusion limited aggregate morphologies including dendritic structures are observed. Dendrite growth promotes physical isolation leading to dead Zn production and reduced cycle life [89–96]. Moreover, high charging current densities lower zinc battery cycle life [97].

There has been a considerable effort to control dendrite growth [98]. Using electrode or electrolyte additives [99–106] and electrolyte convection [88, 107] have demonstrated

dendrite suppression. Electrolyte flow parallel to the electrode surface is claimed to provide ultra-long cycle life of ≈ 18000 cycles with increasing electrolyte flow rate providing increased cycle life [107].

1.5 Thesis Outline

Experimental evidence [44, 80, 88, 107–109] indicates the importance of electrolyte convection in governing dendrite growth. Hence, for the first time, we analyze the effects of electrolyte flow normal and parallel to the electrode on dendrite growth. In chapter 2, we investigate the effect of normal flow on dendrite growth. In chapter 4 we talk about the effect of fully developed creeping flow parallel to the electrodes on dendrite growth. Since SEI growth is an important feature of lithium metal batteries, in chapter 5 we study the effect of normal flow on SEI growth in LMBs. In chapter 3 we study the effect of electrode design parameters such as pore sizes, pore separation, and lithium metal electrode thickness on dendrite growth and energy density while accounting for the temporal changes in shape of the electrode surface. Since zinc metal batteries are another class of emerging batteries that suffer from dendrite growth, in chapter 6 we study the effect of normal flow on dendrite growth on zinc metal electrodes. Finally in chapter 7, we present the conclusions.

Chapter 2

Controlling dendrite growth in lithium metal batteries through forced advection

Following the lead of Tan *et al.* [44], Li *et al.* [43], and Wlasenko *et al.* [109], in this chapter we investigate the effect of advective transport normal to the deposition surface on dendrite growth. Using a first order stability analysis technique, similar to the one used by Tikekar *et al.* [16], we also calculate the dendrite growth rate as a function of normal flow rate and current density.

2.1 Governing Equations

Figure 2.1 shows a schematic diagram of the Li metal cell with electrolyte flow. A charging current density $\tilde{\mathbf{J}}(\mathbf{X}, \mathbf{T})$ transports Li^+ ions from the positive electrode at $Z = 0$ to the Li metal electrode at $Z = L$ where they plate and change the thickness of the anode over time T. The electrodes are assumed to be porous with an imposed electrolyte flow of velocity v along the Z axis. The Li metal electrode could either be perforated or porous (*e.g.* metal foam) to allow normal flow. We assume that the pore structure is

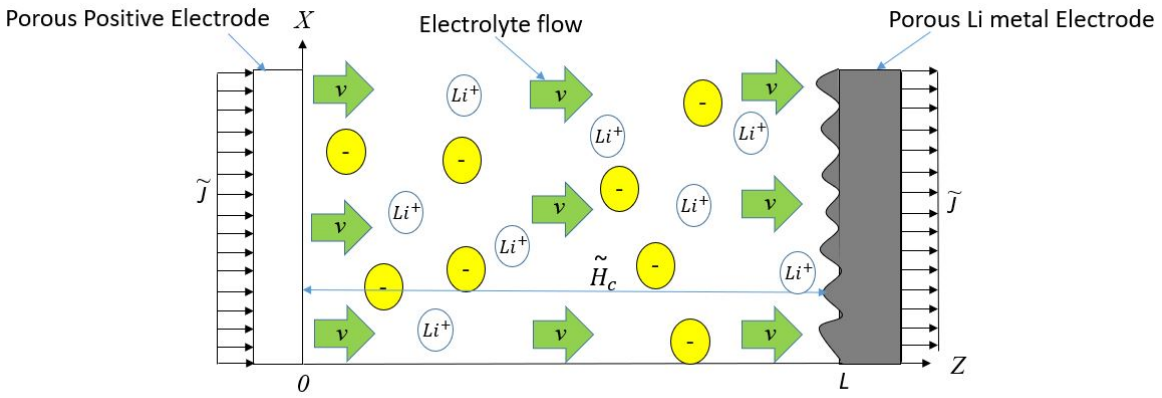

Figure 2.1. Schematic diagram of the lithium metal cell model

sufficiently fine scaled to allow uniform flow.

Within the electrolyte (neglecting the double layer region)

$$\nabla \cdot \tilde{\mathbf{J}} = 0. \tag{2.1}$$

The cation and anion transport equations [16] are given by,

$$\frac{\tilde{\mathbf{J}}}{F} = -D_c \nabla \tilde{C}_c - \mu_c F \tilde{C}_c \nabla \tilde{\Phi} + \tilde{C}_c \mathbf{v} \tag{2.2}$$

and

$$\mathbf{0} = -D_a \nabla \tilde{C}_a + \mu_a F \tilde{C}_a \nabla \tilde{\Phi} + \tilde{C}_a \mathbf{v} \tag{2.3}$$

where F is Faraday's constant, D is diffusivity, μ is electric mobility, $\tilde{C}(X, Z, T)$ is concentration, $\mathbf{v} = v\hat{\mathbf{k}}$, and $\tilde{\Phi}(X, Z, T)$ is electrostatic potential. The subscripts c and a indicate cation and anion respectively. Electroneutrality requires

$$\tilde{C}_c = \tilde{C}_a. \tag{2.4}$$

The growth rate of the Li metal electrode per unit surface area due to electrodeposition is given by

$$\frac{\partial \tilde{H}_c}{\partial T} = \left(\frac{v_m}{F}\tilde{\mathbf{J}} \cdot \tilde{\mathbf{n}}\right)|_{\tilde{H}_c}, \tag{2.5}$$

where $\tilde{H}_c$ is the distance between lithium metal electrode and the positive electrode, v_m is the molar volume of Li, and $()|_{\tilde{H}_c}$ means evaluated at the growing surface $\tilde{H}_c$. Introducing the non dimensional variables, $\tilde{\mathbf{j}} = \frac{\tilde{\mathbf{J}}L}{FD_cC_0}$, $Pe = \frac{vL}{D_c}$, $\tilde{\phi} = \frac{\tilde{\Phi}F}{RT}$, $\tilde{c_c} = \frac{\tilde{C_c}}{C_0}$, $\tilde{c_a} = \frac{\tilde{C_a}}{C_0}$, $z = \frac{Z}{L}$, $x = \frac{X}{L}$, $M = (\frac{Dc}{Da} + 1)$, $\tilde{h_c} = \tilde{H}_c/L$, $k = KL$, and $t = \frac{v_m D_c C_0 T}{L^2}$ in Eqs. 2.1-2.5 produces

$$\nabla \cdot \tilde{\mathbf{j}} = 0, \tag{2.6}$$

$$\tilde{\mathbf{j}} = -\nabla \tilde{c_c} - \tilde{c_c}\nabla\tilde{\phi} + \tilde{c_c} Pe \widehat{\mathbf{k}}, \tag{2.7}$$

$$\mathbf{0} = -\nabla \tilde{\mathbf{c_a}} + \tilde{c_a}\nabla\tilde{\boldsymbol{\phi}} + \tilde{c_a}(MPe - Pe)\widehat{\mathbf{k}}, \tag{2.8}$$

$$\tilde{c_c} = \tilde{c_a}, \tag{2.9}$$

$$\frac{\partial \tilde{h_c}}{\partial t} = \tilde{\mathbf{j}} \cdot \tilde{\mathbf{n}}|_{\tilde{h_c}}, \tag{2.10}$$

where C_0 is the average concentration and $\widehat{\mathbf{k}}$ is the unit vector in z direction.
The electrochemical energy of the cation at the Li metal boundary is

$$\Psi_c(X, \tilde{H}_c, T) = \Psi_c^0 + RT_0 \ln(\tilde{C}_c(X, \tilde{H}_c, T)) + F\tilde{\Phi}(X, \tilde{H}_c, T) \tag{2.11}$$

where Ψ_c^0 is the standard electrochemical energy for the electrolyte, R is the universal gas constant, T_0 is the operating cell temperature, and the electrochemical energy in the Li metal electrode is

$$\Psi_m(X,T) = \Psi_m^0 + \gamma v_m K(X,T) + F\tilde{\Phi}_m(X,T), \tag{2.12}$$

where γ is the surface tension at the electrode-electrolyte interface, Ψ_m^0 is the standard electrochemical energy for the electrode, K is the curvature, and $\Phi_m(X,T)$ is the electrostatic potential at the Li metal electrode surface.

At equilibrium, $\Psi_c = \Psi_m$, so

$$\tilde{\Phi}_m = \frac{\Psi_c^0 - \Psi_m^0}{F} + \frac{RT_0}{F}\ln(\tilde{C}_c(X,\tilde{H}_c,T)) - \frac{\gamma v_m K(X,T)}{F} + \tilde{\Phi}(X,\tilde{H}_c,T) \tag{2.13}$$

The applied charging current density leads to an electrostatic potential of E_0 at the counter-electrode.

$$\tilde{E}_0 = \tilde{\Phi}(X,0,T). \tag{2.14}$$

Non-dimensionalization of Eqs. 2.13 and 2.14 leads us to

$$\tilde{\phi}_m = \psi_c^0 - \psi_m^0 + \ln(\tilde{c_c}(x,\tilde{h_c},t)) - \beta k(x,t) + \tilde{\phi}(x,\tilde{h}_c,t) + 6.91, \tag{2.15}$$

$$\tilde{e}_0 = \frac{\tilde{E}_0 F}{RT_0}, \tag{2.16}$$

$$\tilde{\phi}(x,0,t) = \tilde{e}_0, \tag{2.17}$$

where $k = KL$, $\tilde{\phi}_m = F\tilde{\Phi}_m/(RT_0)$, $\psi_c^0 = \Psi_c^0/(RT_0)$, $\beta = \gamma v_m/(RT_0 L)$, and $\psi_m^0 = \Psi_m^0/(RT_0)$. Thus, the nondimensional model has only five nondimensional parameters: Pe, j, M, k, β.

2.2 Base Case Solutions

For the base case, uniform plating is assumed, so $\tilde{\mathbf{j}}(x,t) = j\widehat{\mathbf{k}}$, $\tilde{c_c}(x,z,t) = c_c(z)$, $\tilde{c_a}(x,z,t) = c_a(z)$, $\tilde{\phi}(x,z,t) = \phi(z)$, $\tilde{e}_0(x,z,t) = e_0$, and $\tilde{h_c}(x,t) = h_c(t)$. Substitution into Eqs. 2.7-2.10 along with $K = 0$ for the planar electrode in base case and using the boundary conditions $c_a(0) = c_{a0}$, $\phi(1) = 0$, and the initial condition $h_c = 1$, and Eq. 2.17 gives the base case solutions

$$c_c = \frac{j}{MPe} + \left[c_{a0} - \frac{j}{MPe}\right] \exp(zMPe/2), \tag{2.18}$$

$$\phi = e_0 + \ln\left[\frac{(c_{a0} - \frac{j}{MPe}) \exp(\frac{(2Pe-MPe)z}{2}) + \frac{j}{MPe} \exp((-MPe + Pe)z)}{c_{a0}}\right], \tag{2.19}$$

$$c_{a0} = \frac{j}{MPe} + \frac{[1 - \frac{j}{MPe}][MPe/2]}{\exp(MPe/2) - 1}, \tag{2.20}$$

$$h_c = 1 - jt. \tag{2.21}$$

Critical Peclet number is defined as the Peclet number at which advective flux equals the total ionic flux at the negative electrode, or

$$j = c_c(1)Pe_{cr}. \tag{2.22}$$

Figures 2.2a, 2.2b, and 2.2c show the concentration, electrostatic potential, and electric field profiles for a given current density and various electrolyte velocities using the parameters listed in Tab. 2.1. The baseline solution without flow ($Pe = 0$) shows the

Property	Value
C_0	$1\ M$
T_0	$300\ K$
L	$1\ mm$
D_a	$4E-10\ m^2s^{-1}$ [16]
D_c	$10^{-11}\ m^2s^{-1}$ [14]
F	$96500\ Cmol^{-1}$
R	$8.314\ Jmol^{-1}K^{-1}$
γ	$1.716\ Nm^{-1}$ [16]
μ_c	$D_c/(RT_0)\ mols^{-1}N^{-1}$
μ_a	$D_a/(RT_0)\ mols^{-1}N^{-1}$
v_m	$1.33E{-}5\ molm^{-3}$ [16]

Table 2.1. Parameters used in the model

concentration decreasing, from the positive electrode to the lithium metal electrode. The electrostatic potential decreases from $\phi(0) = 1$ to the boundary condition, $\phi(1) = 0$. The electric field increases with a maximum at the negative electrode. These results agree with previous research [16]. Increasing the velocity reduces the concentration, electrostatic potential gradients, and the electric field from the baseline case of $Pe = 0$. At $Pe = Pe_{cr}$, the ion concentration is almost uniform at $c_c = 1$, $\phi = 0$, and $d\phi/dz = 0$. Increase of Pe above Pe_{cr} reverses the concentration and electrostatic potential gradients. Figure 2.2b shows that higher flow rates lower the electrostatic potential at the counter-electrode surface. This phenomenon stems from the fact that some of the energy required to move the Li^+ ions from the counter-electrode to the Li metal electrode is supplied by the fluid flow, thus reducing the required electrical power.

Figures 2.3a, 2.3b, and 2.3c show the concentration, electrostatic potential, and electric field at a given flow rate ($Pe = 0.5$) and various charging current densities. Higher current leads to higher concentration and electrostatic potential gradients at the Li metal electrode surface. Thus, diffusion and migration fluxes are higher at higher current densities and potentially can lead to higher dendrite growth rates. [3, 16].

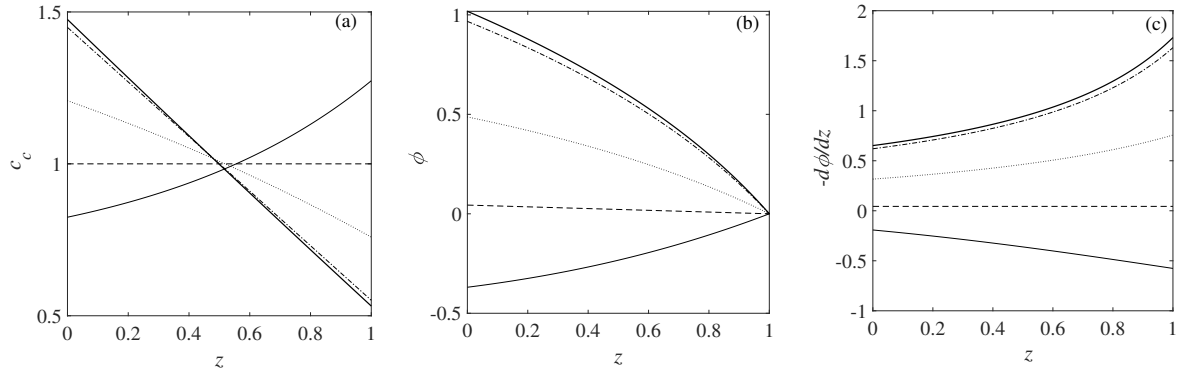

Figure 2.2. Base case solutions of non-dimensionalized (a) Concentration, (b) electrostatic potential and (c) Electric field at $j = 1.8$: $Pe = 1.5Pe_{cr}$ (solid), $Pe = Pe_{cr}$ (dashed), $Pe = 0.5Pe_{cr}$ (dotted), $Pe = 0$ (dashed-dotted), and $Pe = -0.05Pe_{cr}$ (bold).

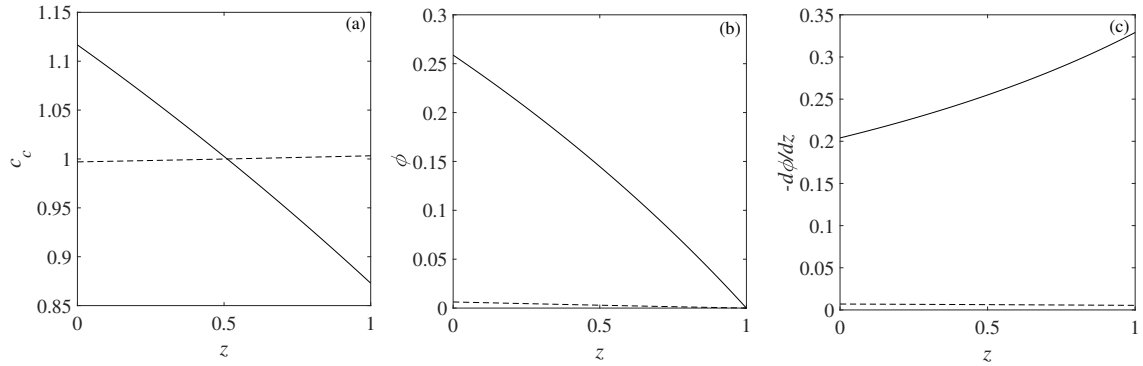

Figure 2.3. Base case solutions of non-dimensionalized (a) Concentration, (b) electrostatic potential, and (c) Electric field at $Pe = 0.5$, $M = 0.51$ for $j = 0.5$ (dashed) and $j = 1$ (solid).

Figure 2.4 shows the critical Peclet number versus j. For small j, the concentration is approximately uniform, so $c_c(1) = 1$ and $j = Pe_{cr}$. The critical Peclet number is on the order of 1, so the dimensional critical velocity is on the order of D_c/L. For $j = 1.8$ and parameters in Table 2.1, the critical velocity is roughly 1.75 $nm\ s^{-1}$ which means that the fluid particles would take approximately a week to cross the inter-electrode gap by advective flux. $j = Pe_{cr}$ implies that we need only 37 mL/Ah of flow volume. Thus, the required flow rate is very low and may be practically achieved using a variety of low power methods. As shown in Fig. 2.4, the critical Peclet number is independent of temperature. It depends only on current density. The critical velocity, however, reduces with reducing temperature because the diffusivity reduces with reducing temperature [14].

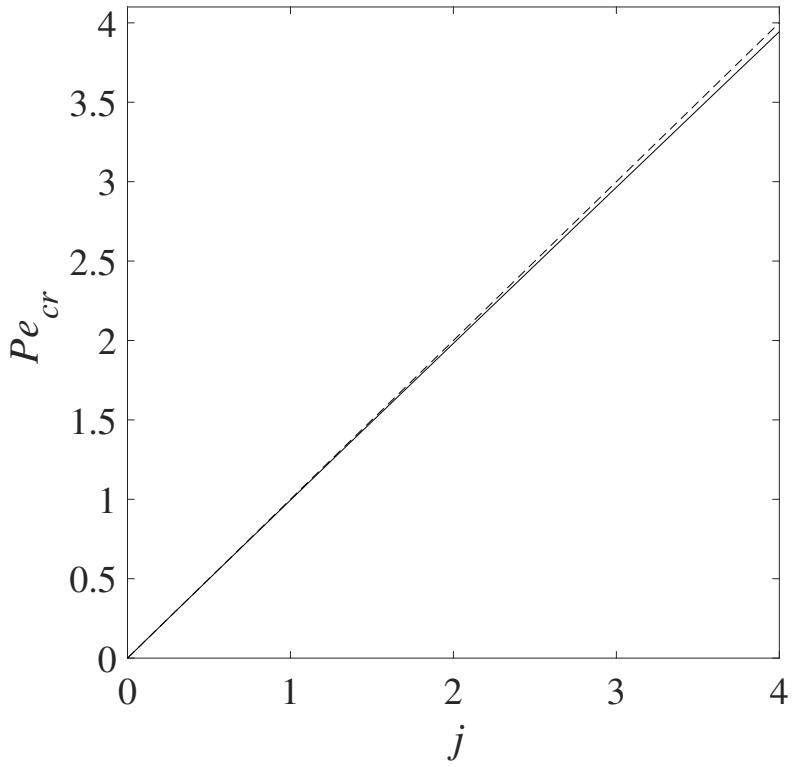

Figure 2.4. Critical Peclet number versus non-dimensional current density (solid) and a linear approximation (dashed).

2.3 Stability analysis

To analyze the stability of electroplating on the Li metal surface, we introduce the first order sinusoidal perturbation,

$$\tilde{h_c} = h_c + h_c' exp(\sigma t) exp(ikx), \tag{2.23}$$

where k, h_c' and σ are the non-dimensional wavenumber, non-dimensional amplitude, and non-dimensional exponential growth rate. The wavenumber equals $2\pi/\lambda$ where λ is the wavelength. Dendrites are assumed to grow exponentially fast for σ greater than 0 and

decay for σ less than 0. To eliminate dendrites, the electrode must be stable ($\sigma < 0$) for dendrites of all sizes (k). The perturbation growth rate (σ) is a function of wavenumber (k) as dendrites with different curvatures may grow with different rates due to the effect of surface tension, varying concentration of electric field lines, and varying concentration gradient on the curved dendrite tip. The positive electrode surface at $z = 0$ has not been perturbed because no dendrites grow from the positive electrode during charging.

The concentration, electrostatic potential, and current density are assumed to have the same spatial and temporal dependencies:

$$\tilde{c_c} = c_c + c_c' exp(\sigma t) exp(ikx), \tag{2.24}$$

$$\tilde{\phi} = \phi + \phi' exp(\sigma t) exp(ikx), \tag{2.25}$$

$$\tilde{\mathbf{j}} = j\widehat{\mathbf{k}} + \mathbf{j}' exp(\sigma t) exp(ikx), \tag{2.26}$$

where c_c', ϕ', and j' are the non-dimensional amplitudes of the perturbations in cation concentration, electrostatic potential, and current density respectively. We assume that the porous electrodes are sufficiently thick and that the electrolyte storage tank is sufficiently far enough. Using Darcy's law in the porous electrode, creeping flow in the gap between two electrodes, continuity of pressure and velocity perturbations across the porous electrode-electrolyte interface, and zero pressure and velocity perturbations at the outlet of porous electrode and in the electrolyte storage tank drives velocity perturbations throughout the domain to zero.

Substitution of Eqs. 2.24-2.26 into Eqs. 2.7- 2.9 yields

$$\phi' = \frac{c_c'}{c_c} \tag{2.27}$$

Eqs. 2.26 and Eq. 2.10 imply

$$\sigma h_c' = 2\frac{dc_c'}{dz}(1) - MPec_c'(1) \tag{2.28}$$

Eqs. 2.11, 2.12 give

$$\frac{c_c'(1)}{c_c(1)} + \frac{1}{c_c(1)}\frac{dc_c}{dz}(1)h_c' + \phi'(1) + \frac{d\phi}{dz}(1)h_c' = -\beta h_c' k^2 \tag{2.29}$$

Solving the above equations leads to the following solution for the perturbation growth rate σ

$$\sigma = \frac{c_c(1)}{2}\left[\frac{-1}{c_c(1)}\frac{dc_c}{dz}(1) - \frac{d\phi}{dz}(1) - \beta k^2\right]\left[2\frac{m_1 exp(m_1) - m_2 exp(m_2)}{exp(m_1) - exp(m_2)} - MPe\right], \tag{2.30}$$

where $m_1 = \frac{MPe+\sqrt{M^2Pe^2+16k^2}}{4}$ and $m_2 = \frac{MPe-\sqrt{M^2Pe^2+16k^2}}{4}$.

Equation 2.30 shows that a higher value of β implies lower perturbation growth rate at the same wavenumber and flow rate. β depends on surface energy γ and molar volume v_m and hence a higher surface energy implies lower perturbation growth rate. This is intuitive because higher γ makes it more difficult to have curved dendritic deposits. Sundstrom *et al.* [15] also show that increasing surface energy leads to a reduced perturbation growth rate. However, increasing surface energy has no effect on the critical flow rate, as critical flow rate is derived from the base case solutions which are independent

of β. Critical wavenumber,

$$k_{cr} = \sqrt{\frac{1}{\beta}\left[\frac{-1}{c_c(1)}\frac{dc_c}{dz}(1) - \frac{d\phi}{dz}(1)\right]}, \tag{2.31}$$

is the wavenumber above which $\sigma < 0$.

Figure 2.5 shows the non-dimensional dendrite growth rate at a given current density and various flow rates versus non-dimensional wavenumber.

$$c_c'(1) = h_c'\frac{c_c(1)}{2}\left[\frac{-1}{c_c(1)}\frac{dc_c}{dz}(1) - \frac{d\phi}{dz}(1) - \beta k^2\right] \tag{2.32}$$

$$c_c'(1) = 0.5h_c'\left[j - Pec_c(1) - \beta k^2 c_c(1)\right] \tag{2.33}$$

Equations 2.32 and 2.33 show that increasing the flow rate reduces the magnitude of $c_c'(1)$, thus leading to more uniform concentration distribution near the lithium metal electrode-electrolyte interface. This promotes uniform plating and reduces dendrite growth.

For a given charging current and a flow rate, σ increases with k and then decreases. This is because with increasing curvature, the concentration of electric field lines and the concentration gradient at the dendrite tip increase, leading to higher dendrite growth. However, as can be seen from Eq. 2.12, higher k also increases the required surface energy per mole of electrodeposited Li and thus acts as a deterrent to the increase of σ with k. In agreement with Tikekar *et al.* [16], the zero flow case has an unstable Li metal electrode ($\sigma > 0$) for $k < 597$. Flow towards the Li metal electrode during charging reduces the dendrite growth rate. In fact, above the critical flow rate, σ <0 for all wavenumbers. In other words, supercritical flow can entirely stabilize the Li metal elec-

trode. For supercritical flow rates, sum of first two terms (including - sign) in the first bracket in Eq. 2.30 is negative. Since, β and k are always positive and since the second bracket of Eq. 2.30 and $c_c(1)$ are always positive for reasonable flow rates, supercritical flow ensures negative perturbation growth rate for all wavenumbers including zero. So, even though M is an important model parameter it does not influence the fact that for stable plating for all wavenumbers, supercritical flow is required. Subcritical flow rates may not completely stabilize the electrode but the peak height and range of unstable wavenumbers ($k < k_{cr}$) are both reduced, thus reducing the level of electrode instability. If the critical wavenumber is sufficiently small, then the size of the unstable growth will be large and not dendritic, potentially exceeding the physical size of the electrode and eliminating dendrite growth as a practical concern. Flow in the wrong direction, however, can enhance the dendrite growth rate.

This model does not explicitly account for breakage and reformation of SEI. SEI breakage occurs due to multiple reasons, including the large volume change associated with plating and stripping Li from under the SEI and excessive tensile stress at the dendrite tips. Large volume changes can lead to inhomogeneities in the SEI layer that may initiate dendrites. At the dendrite tips, SEI may fail under excessive tensile stress [2]. The stress itself depends on curvature. For sinusoidal perturbations with infinitesimally small amplitude studied in this work, the dendrite tip curvature is proportional to the amplitude and the square of the wavenumber. For low wavenumbers, the curvature is infinitesimally small and the tensile stress on the SEI at the dendrite tips is infinitesimally small, so, the SEI will not break. In regions where the electrode is stable, the small initial perturbations decay with time.

Table 2.2 explains the stabilizing effect of normal flow. Diffusion, migration and ad-

Pe/Pe_{cr}	Diffusion	Migration	Advection	σ_{max}	k_{cr}
-0.05	0.514	0.513	-0.0264	437	615
0	0.5	0.5	0	413	597
0.5	0.307	0.316	0.378	176	403
1.	-0.0125	0.0125	1	1.15	69
1.5	-0.482	-0.434	1.91	-0.734	0

Table 2.2. Normalized Li^+ ion flux contributions at $z = 1$ and maximum non-dimensionalized perturbation growth rate versus flow rate for $j = 1.8$

vection flux add together to produce the total Li^+ ion flux at different flow velocities. Increasing the flow rate increases the contribution of advection relative to migration and diffusion. Thus, increasing flow rate in the direction of total flux helps reduce dendrite growth rate and critical wavenumber. This result is in agreement with the explanation for dendrite growth rate given by Aryanfar et al. [22]. At the critical velocity ($Pe = Pe_{cr}$), total flux equals the advective flux at the lithium metal electrode, so diffusion and migration fluxes sum to zero. As shown by dashed line for critical velocity in Fig. 2.5, this totally eliminates dendrite growth. However, in Tab. 2.2, the small value of $\sigma = 1.15$ at $Pe = Pe_{cr}$ is because of numerical error. In fact, if advective flux is more than total flux the dendrites dissolve instead of growing.

Figure 2.6 shows the non-dimensional perturbation growth rate versus k for a given flow rate at various current densities. Higher current leads to higher growth rate at the same wavenumber. This result is as per the expectations because at zero current, the dendrite growth rate should be zero.

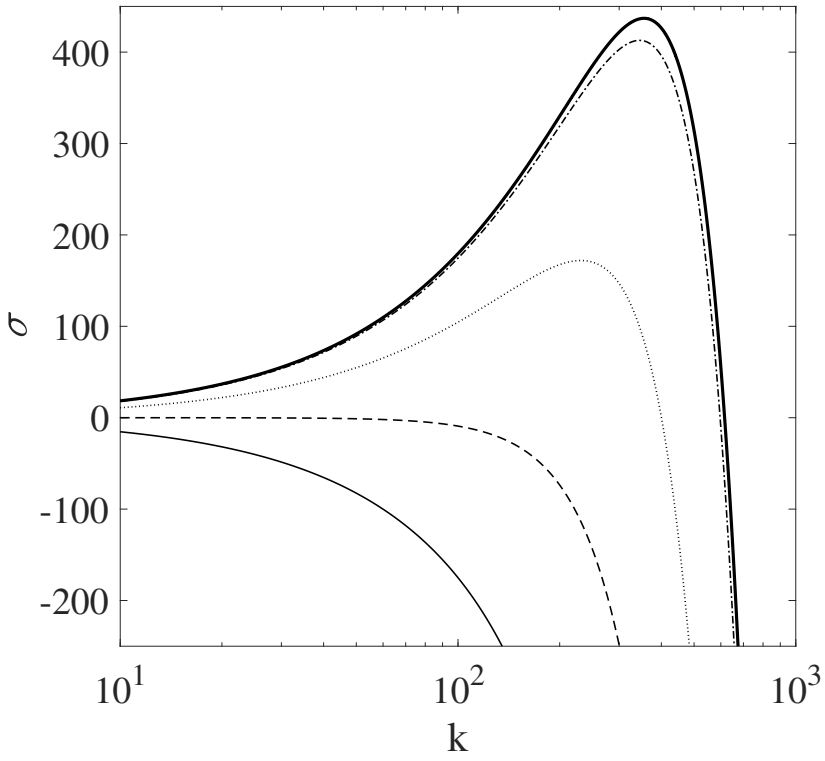

Figure 2.5. Non-dimensional growth rate vs non-dimensional wavenumber at $j = 1.8$, $Pe = 1.5Pe_{cr}$ (solid), $Pe = Pe_{cr}$ (dashed), $Pe = 0.5Pe_{cr}$ (dotted), $Pe = 0$ (dashed dotted), and $Pe = -0.05Pe_{cr}$ (bold).

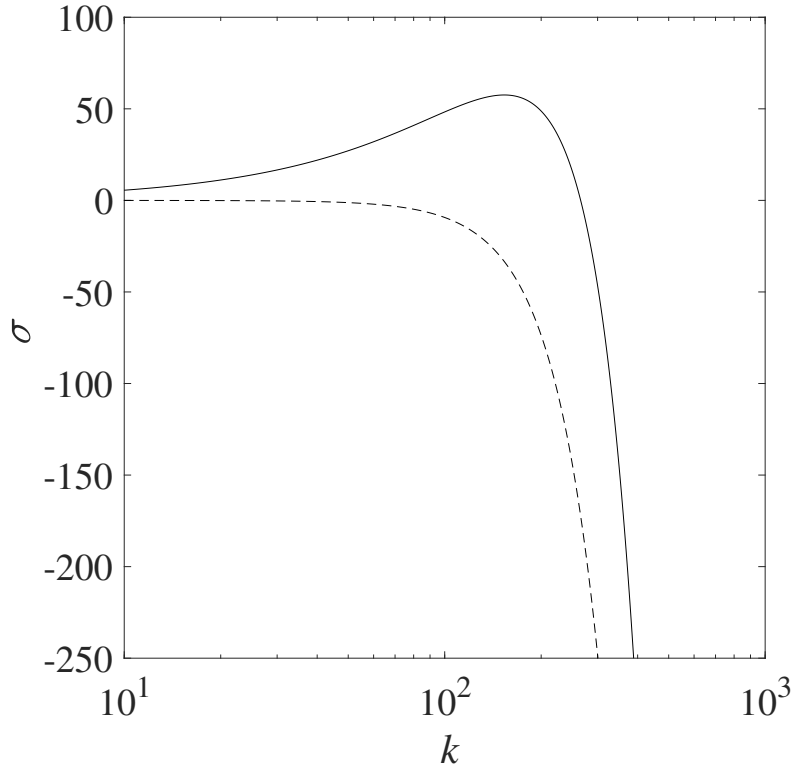

Figure 2.6. Non-dimensional growth rate vs non-dimensional wavenumber at $Pe = 0.5$, $M = 0.51$, $j = 2j_{cr}$ (solid) and $j = j_{cr}$ (dashed). Here j_{cr} is defined as the value of j for which $Pe = 0.5 = Pe_{cr}$.

Chapter 3

Dendrite suppression and energy density in metal batteries with electrolyte flow through perforated electrodes

This chapter considers the effect of electrode microstructure on the velocity profile, dendrite growth, and energy density of LMBs. We study the effect of rectangular slots in the electrode on the flow field and metal plating distribution evolution in time.

3.1 Model development

We build a 2D model with a deforming electrode geometry using the electrodeposition module [110] and creeping flow interface of the CFD module [111] of COMSOL Multiphysics ® software [112]. Figure 3.1 shows the 2D model for a single hole (slot) in the lithium metal electrode surface. The inter-electrode gap is set to 1 mm.

The electrolyte density is 1300 kg/m^3 [113], and dynamic viscosity is 4.152E-3 Pa/s [114].

The cation and anion diffusion coefficients are 1E-11 m^2/s [16] and 4E-10 m^2/s [14], respectively. Both the cations and anions have charge number equal to 1. We assume the exchange current density to be 0.943 A/m^2 [115]. The cathodic and anodic charge transfer coefficients are assumed to be 0.5 each.

We neglect the small double layer regions and assume the electrolyte to be electrically neutral. Concentration dependent electrode kinetics is used to link the concentration, local current density and the activation overpotential at the electrode surfaces.

In order to account for the numerous slots present in the lithium metal electrode surface, we use symmetry boundary conditions on the left and right. We assume a constant charging current density of 1 A/m^2 at the positive electrode surface. The negative electrode is assumed to be grounded. This allows us to identify regions where more plating occurs and also to maintain charge balance. The positive electrode is assumed to be porous and has a constant inlet velocity boundary condition. The slot boundary has a pressure outlet boundary condition with pressure set to 0. The negative electrode surface also has a deforming electrode boundary condition to account for the change in shape of the electrode surface due to electrodeposition of Li ions. This also helps us to observe pore blockage with increasing electrodeposition time.

We assume that the electrolyte has a uniform concentration of 1 M, initially. The initial velocity v is assumed to be uniform with its value being the inlet velocity. The initial pressure is assumed to be zero. We assume a uniform electrostatic potential of 25 mV.

Using the model geometry shown in Fig. 3.1, the mentioned parameter values, the

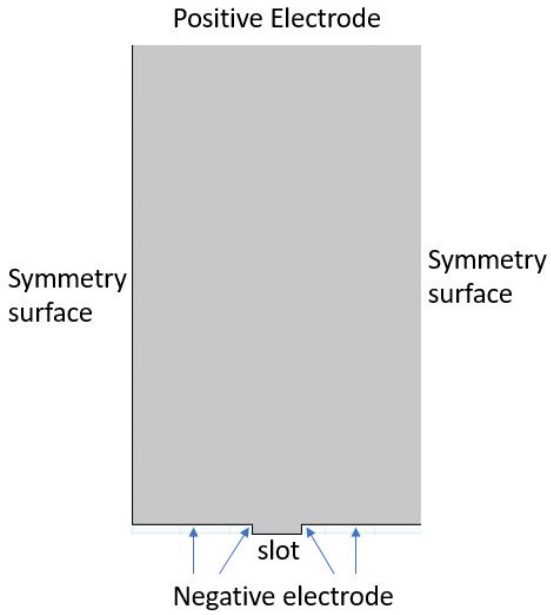

Figure 3.1. Schematic

initial conditions, and the boundary conditions we solve for the flow field. The flow field is then used as an input to solve for the concentration and overpotential. We choose to solve for the first 1000 seconds of the charging process. This is because, our target is to obtain dendrite free plating as early as possible in the charging process. Choosing just the first 1000 seconds still leaves a large chunk of typical battery charging time of 1.5 hrs. A time step of 5 s and an extremely fine triangular mesh with the following mesh parameters is used for our simulations (maximum element size: 1.1E-5 m, minimum element size: 8.25E-8 m, maximum element growth rate: 1.2, curvature factor: 1, resolution of narrow regions: 1) In order to study the effect of flow rate and electrode geometry on the electrodeposition proceess we run simulations for differenr values of v, electrode thickness T_e, slot width W_s ,and inter-slot gap W_d.

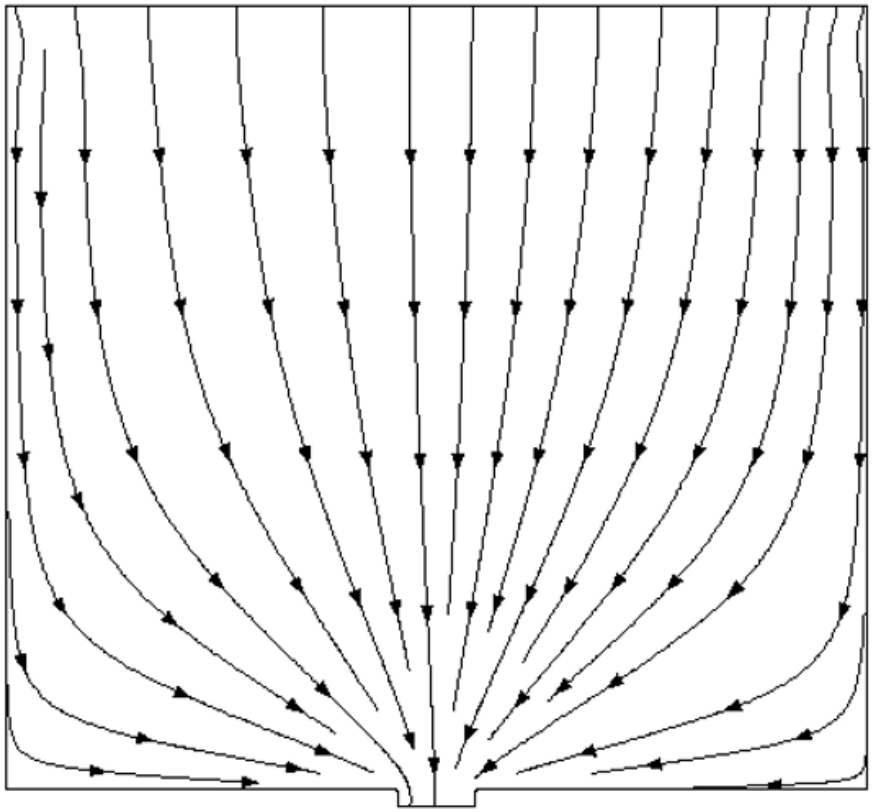

Figure 3.2. Electrolyte flow streamlines

3.2 Results

Fig. 3.2 shows the velocity streamlines. Since, we are in the creeping flow regime, the velocity field does not change much with time. With the inlet velocity being uniform and perpendicular to the positive electrode, the streamlines are evenly spaced and are normal near the inlet. Due to the no penetration boundary condition at the negative electrode, the streamlines turn towards the slot. Since, a lot of streamlines come close near the slot, the velocity gradient near the slot is high. Moreover, the velocities are also high near the slot as the outlet area is lower compared to the inlet area.

Fig. 3.3 shows the evolution of concentration throughout the electrolyte domain with time for stationary electrolyte and for an inlet electrolyte velocity of 10 nm/s. It shows

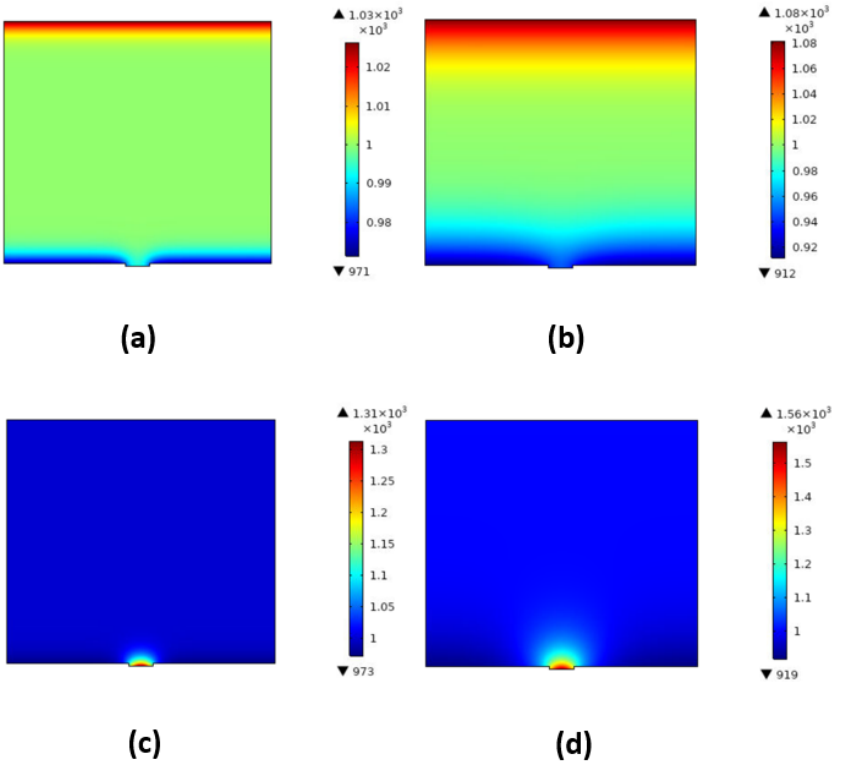

Figure 3.3. Evolution of lithium concentration with time for $W_s = 0.1\ mm$, $W_d = 1\ mm$ and $T_e = 10\ \mu m$: (a) $t = 100\ s$, $v = 0\ nm/s$, (b) $t = 1000\ s$, $v = 0\ nm/s$, (c)$t = 100\ s$, $v = 10\ nm/s$, (d)$t = 1000\ s$, $v = 10\ nm/s$.

that for no electrolyte flow, the concentration profile evolution is similar to a time dependent diffusion profile. However, increasing the electrolyte velocity changes the concentration profile by reducing the diffusion component in the interior of the electrolyte (see chapter 2). However, since the negative electrode surface is impermeable to flow, the flux requirements at the negative electrode surface are met by diffusion. This explains the concentration gradients near the negative electrode surface. With increasing time, the flowing electrolyte tends to drive the lithium ions towards the slots and hence the concentration of lithium ions in the slot increases with time. Since, the flowing electrolyte tends to carry lithium ions with itself, the concentration of lithium ions is highest in the slot.

Figures 3.4 and 3.5 show the variation of oxidation current density along the arc length of one half of the negative electrode. 0 on the x-axis corresponds to the center point of the inter-slot gap. Since, figures 3.4 and 3.5 have been plotted for $W_d = 1\ mm$, arc length of 0.0005 m corresponds to the corner formed by horizontal and vertical surfaces of the negative electrode. During charging lithium ions are reduced to lithium which is plated on the electrode. So, negative and positive oxidation current densities imply lithium ion plating and stripping respectively. A comparison of figures 3.4 and 3.5 shows that increasing the electrolyte velocity increases the amount of plating taking place inside the slot and reduces the plating current density in the inter-slot gap. This is beneficial because high plating current densities in the inter-slot gap can give rise to dendrites which could grow perpendicularly towards the positive electrode and thus increase the chances of an internal short. High plating current density in the slot can also lead to large dendrite growth, but these dendrites would grow parallel to the positive electrode and thus we do not need to worry about any dendritic growth in the slot. Thus, increasing the electrolyte velocity seems to be beneficial.

For non-zero electrolyte velocities, in the inter-slot gap, maximum plating seems to occur near the edge of the slot because flowing electrolyte tends to drive lithium ions towards the slot. For the same reason, plating current density is maximum near the bottom of the slot and hence maximum plating takes place near the bottom of the slot.

With time, plating current density in the inter-slot gap decreases and the plating current density in the slot increases. Eventually, plating current density in the inter-slot gap will become negative (positive oxidation current density) and will lead to stripping in the inter-slot gap. Higher the inlet electrolyte velocity, lower the time required for stripping to begin in the inter-slot gap. Since, the flowing electrolyte tends to drive

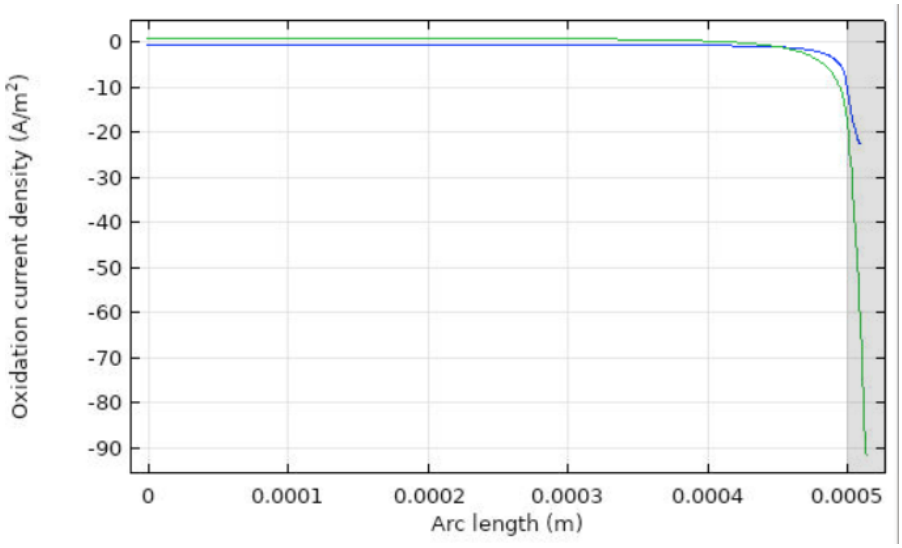

Figure 3.4. Oxidation current density along negative electrode (unshaded: inter-slot gap, shaded: slot) at 100 s (blue) and 1000 s (green) for $v = 300\ nm/s$, $T_e = 10\ \mu m$, $W_d = 1\ mm$, and $W_s = 0.1\ mm$.

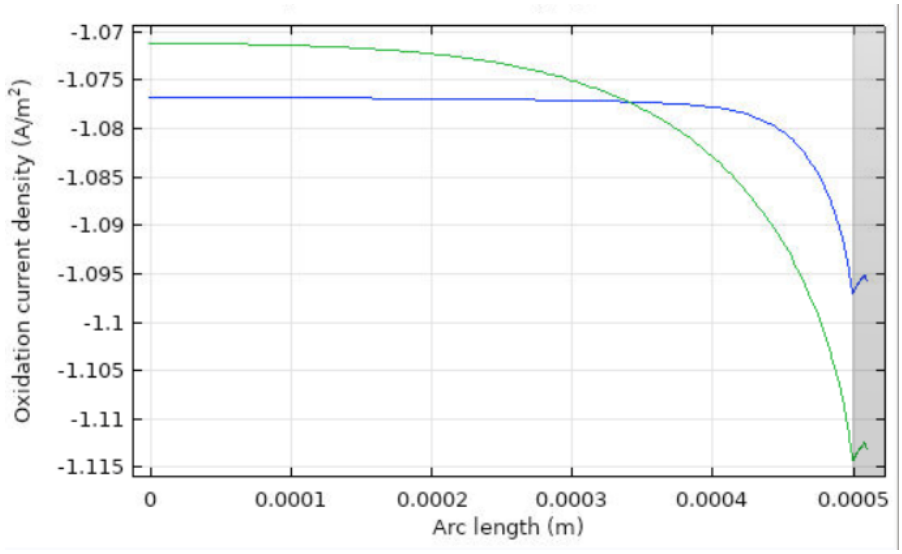

Figure 3.5. Oxidation current density along negative electrode (unshaded: inter-slot gap, shaded: slot) for stationary electrolyte at 100 s (blue) and 1000 s (green) for $v = 0\ nm/s$, $T_e = 10\ \mu m$, $W_d = 1\ mm$, and $W_s = 0.1\ mm$.

the ions towards the slot, the plating current density is the least at the center of the inter-slot gap. So, stripping always begins at the center of the inter-slot gap. Dendrite width is typically of the order of 1 μm or lower. So, anything wider than 10 μm may not be called a dendrite. In order to determine if the plating is dendritic or not, we

use the critical wavenumber k_{cr} defined in chapter 2 and Tikekar *et al.* [16] for plating with and without electrolyte flow, respectively. The formula for critical wavenumber given in chapter 2 and Tikekar *et al.* [16] is the same. In the work presented in this chapter, even though the electrolyte is allowed to flow, the velocity is zero at the lithium metal electrode surface. So, the physical conditions used in this chapter are between the limiting conditions described in chapter 2 and Tikekar *et al.* [16]. Since, both chapter 2 and Tikekar *et al.* [16] have the same formula for critical wavenumber, we also use the same formula for critical wavenumber. If, the critical wavenumber is smaller than 10^5, then the characteristic width of the electrodeposited Li (π/k_{cr}) would be larger than 10 μm, and thus it would be non-dendritic. Using this criteria, we determine $Persta$ for various inter-slot gaps, electrode thicknesses and slot widths.

Table 3.1 shows the effect of W_d, T_e, and W_s on the portion of the inter-slot gap experiencing non-dendritic plating $Persta$. Increasing the electrode thickness increases the surface area available for plating, thus reducing the average plating current density. This reduces k_{cr} and hence a larger portion of the inter-slot gap experiences non-dendritic plating. Larger slot separation increases the ratio of area available for plating to the area of the positive electrode and thus on an average reduces the plating current density. This increases chances of non-dendritic plating. Increasing the slot-width correspondingly increases the area of the positive electrode but does not affect the surface area available for plating. So, on an average the plating current density increases leading to an increase in the amount of plating in the inter-slot gap. This exacerbates the problem of dendrite growth. Although, this implies that lower slot widths are preferred, very low slot widths could also lead to slot clogging and flow blockage.

Slots in the electrode maybe created by using microneedles or lithography. Lithogra-

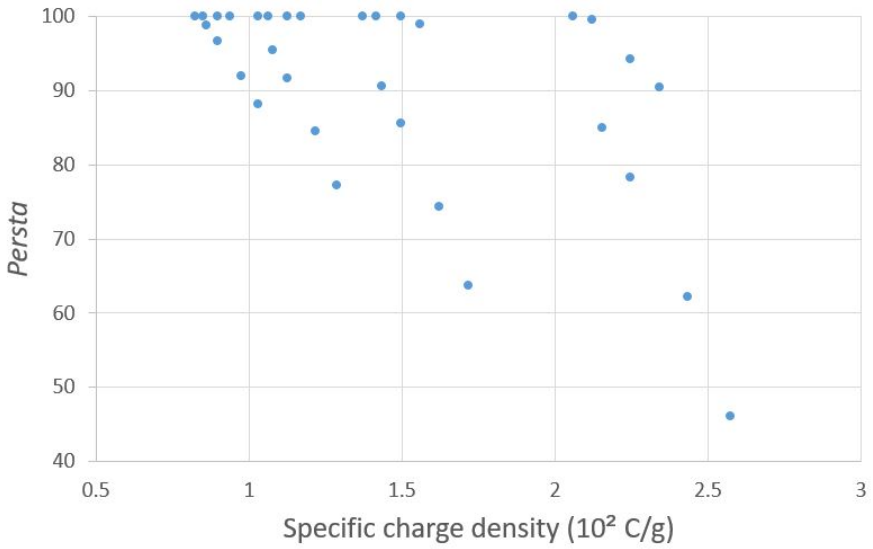

Figure 3.6. Tradeoff between specific charge density and portion of dendrite free inter-electrode gap

phy allows us to create micropatterns with widths as small as a few nanometers [116]. However, our simulations suggest that for an electrolyte inlet velocity of 100 nm/s (which is 10 times the critical velocity described in chapter 2), a slot which was originally 0.075 mm wide experiences a 33 % reduction in width at its narrowest point after 1 hour of charging. This can significantly increase the pressure required to pump the electrolyte. Since, batteries typically take 1 to 1.5 hours to charge completely, it is not desirable to decrease the slot width further.

Fig. 3.6 shows the tradeoff between achieving dendrite free inter-slot gap and stored charge density (for the lithium metal electrode). We are using charge density as a proxy for energy density. This is because introduction of electrolyte velocity leads to a reduction in the charging overpotential and thus reduces the required charging voltage for galvanostatic charging. However, using this reduced voltage would be misleading as the remainder of the energy comes from the kinetic energy of the flowing electrolyte. To calculate the charge density we assume unit cell depth into the plane of the paper.

Table 3.1. Effect OF W_d, T_e, and W_s on $Persta$ at $t = 1000\ s$ and $v = 200\ nm/s$

$W_d\ (mm)$	$T_e\ (\mu m)$	$W_s\ (mm)$	$Persta$
0.4	10	0.1	90.5
0.4	10	0.15	46.08
0.4	15	0.1	98.99
1	10	0.1	100

The density of lithium is assumed to be 534 kg/m^3 [117]. Thus, the specific charge density has been calculated relative to mass of the lithium metal that is present in the negative electrode before deposition begins. It does not consider mass of the electrodeposited lithium. So, it won't be fair to compare this to the theoretical specific capacity of lithium (3860 mAh/g), which is calculated by just considering the mass of the electrodeposited lithium and not the mass of the negative electrode before electrodeposition begins. Fig. 3.6 shows that specific charge density as high as 206 C/g maybe achieved for a completely dendrite free inter-slot gap. Such high charge density has been possible, because of the low electrode thickness. The high inter-slot gap and lower slot widths help in achieving non-dendritic plating in the inter-slot gap but they also ensure that the charge density is not the highest. This indicates the presence of a tradeoff between charge density and the ability to achieve non-dendritic plating.

Chapter 4

Reducing dendrite growth in lithium metal batteries by creeping Poiseuille and Couette flows

In this chapter we analyze the effect of an electrolyte flowing parallel to the electrode surface. We study the effect of creeping Poiseuille and Couette flows (see Fig. 4.1) on dendrite growth in lithium metal batteries.

4.1 Governing Equations

Figure 4.1 shows a schematic diagram of a Li metal cell with advective electrolyte flow parallel to the electrodes. Poiseuille flow and Couette flow have the parabolic and linear velocity profiles shown in Fig. 4.1a and Fig. 4.1b, respectively. Poiseuille flow may be generated by externally pumping the electrolyte through the inter-electrode gap using a pressure gradient in the $\mathbf{X}$ direction. Couette flow can be generated by relative horizontal motion of the two electrodes.

With Couette and Poiseuille flow being parallel to the electrode, diffusion is the main

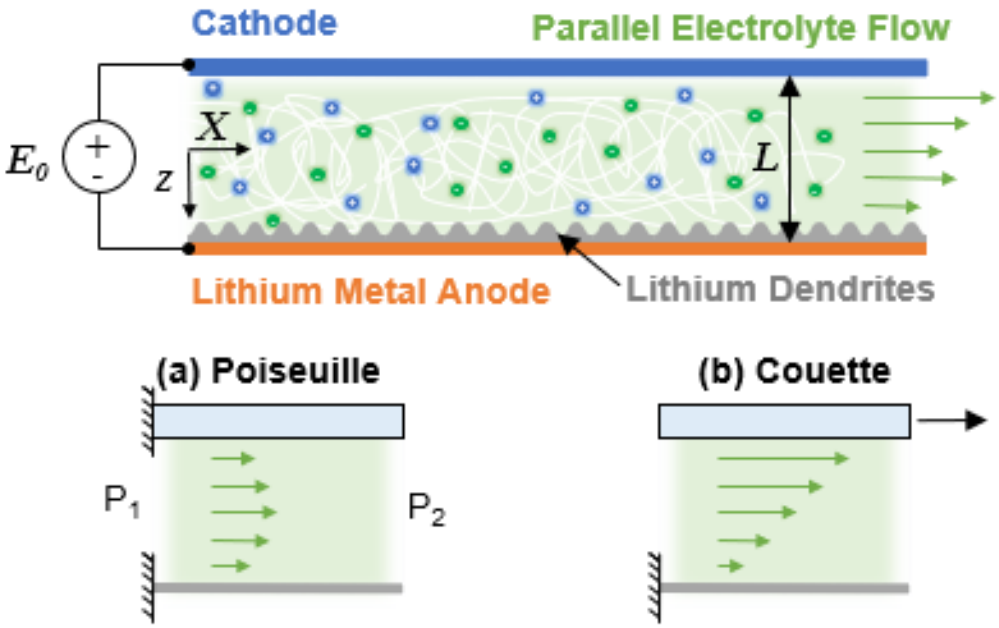

Figure 4.1. Schematic diagram of the lithium metal cell with (a) Poiseuille flow and (b) Couette flow.

ion transport mechanism. The time scale for an ion to move from one electrode to the other may be given by L^2/D_c, where L is the inter-electrode distance and D_c is the diffusivity of cations. For the parameters listed in 1, this time is 40 s. Typically batteries take around an hour to charge and thus, 40 s is negligible compared to the timescale of charging process. Moreover, electrolyte flow is assumed to be creeping flow and so it is quasistatic. In case of Couette flow, the creeping flow assumption means that flow has negligible transients and tracks the relative motion of the two electrodes. So, the relative motion can be periodic in nature without a steady drift of one electrode relative to the other.

A charging current density $\tilde{J}(X,T)$ transports Li^+ ions from the positive electrode at $Y = -0.5L$ to the Li metal electrode at $Y = 0.5L$ where they plate and change the thick-

ness of the anode over time T. In both cases, electrolyte flow is parallel to the electrode, so diffusion is the main mechanism for lithium ion transport from the counter-electrode to the lithium metal electrode.

Assuming quasi-steady state gives

$$\nabla \cdot \tilde{\mathbf{N}}_{\mathbf{c}} = 0, \tag{4.1}$$

where

$$\tilde{\mathbf{N}}_{\mathbf{c}} = -D_c \nabla \tilde{C}_c - \mu_{0c} F \tilde{C}_c \nabla \tilde{\Phi} + \tilde{C}_c \tilde{\mathbf{V}} \tag{4.2}$$

is the cation flux where F is Faraday's constant, D is diffusivity, μ_0 is electric mobility, $\tilde{C}(X, Z, T)$ is concentration, $\tilde{\Phi}(X, Z, T)$ is electrostatic potential, and subscript c indicates cation parameters. The anion flux

$$\tilde{\mathbf{N}}_{\mathbf{a}} = -D_a \nabla \tilde{C}_a + \mu_{0a} F \tilde{C}_a \nabla \tilde{\Phi} + \tilde{C}_a \tilde{\mathbf{V}} \tag{4.3}$$

is governed by

$$\nabla \cdot \tilde{\mathbf{N}}_{\mathbf{a}} = 0, \tag{4.4}$$

where subscript a indicates anion parameters. Neglecting the small double layer region, we assume electroneutrality, so

$$\tilde{C}_c = \tilde{C}_a. \tag{4.5}$$

The flow field is described by continuity

$$\nabla \cdot \tilde{\mathbf{V}} = 0, \tag{4.6}$$

and the creeping flow equation

$$-\nabla \tilde{P} + \mu \nabla^2 \tilde{\mathbf{V}} = 0, \tag{4.7}$$

where μ is the dynamic viscosity of the electrolyte, $\tilde{P}(X, Z, T)$ is the pressure, and $\tilde{\mathbf{V}}(X, Z, T)$ is the electrolyte velocity.

The normal anion flux at the lithium metal electrode is assumed to be zero. So,

$$\tilde{\mathbf{N}}_\mathbf{a} \cdot \tilde{\mathbf{n}}|_{\tilde{H}_c} = 0, \tag{4.8}$$

where $\tilde{H}_c$ is the location of lithium metal electrode, $\tilde{\mathbf{n}}$ is the unit vector in a direction normal to the lithium metal electrode surface, and $()|_{\tilde{H}_c}$ means evaluated at the growing surface $\tilde{H}_c$. The rate of electrodeposition per unit surface area of the metal electrode is given by

$$\frac{\partial \tilde{H}_c}{\partial T} = \left(v_m \tilde{\mathbf{N}}_\mathbf{c} \cdot \tilde{\mathbf{n}} \right) |_{\tilde{H}_c}, \tag{4.9}$$

where v_m is the molar volume of Li. Introducing the non dimensional variables, $\tilde{\mathbf{n}}_\mathbf{c} = \frac{\tilde{\mathbf{N}}_\mathbf{c} L}{D_c C_0}$, $\tilde{\mathbf{n}}_\mathbf{a} = \frac{\tilde{\mathbf{N}}_\mathbf{a} L}{D_a C_0}$, $Pe = \frac{V_0 L}{D_c}$, $Re = \frac{\rho V_0 L}{\mu}$, $\tilde{p} = \frac{\tilde{P} L^2}{\mu D_c}$, $\tilde{\mathbf{v}} = \frac{\tilde{V}}{V_0}$, $\tilde{\phi} = \frac{\tilde{\Phi} F}{RT}$, $\tilde{c}_c = \frac{\tilde{C}_c}{C_0}$, $\tilde{c}_a = \frac{\tilde{C}_a}{C_0}$, $z = \frac{Z}{L}$, $x = \frac{X}{L}$, $M = (\frac{Dc}{Da} + 1)Pe$, $\tilde{h_c} = \tilde{H}_c / L$, and $t = \frac{v_m D_c C_0 T}{L^2}$ in Eqs. 4.1-4.9 produces

$$\nabla \cdot \tilde{\mathbf{n}}_\mathbf{c} = 0, \tag{4.10}$$

$$\nabla \cdot \tilde{\mathbf{n}}_\mathbf{a} = 0, \tag{4.11}$$

$$\nabla \cdot \tilde{\mathbf{v}} = 0, \tag{4.12}$$

$$-\frac{\nabla\tilde{p}}{RePe}+\frac{\nabla^2\tilde{\mathbf{v}}}{Re}=0, \tag{4.13}$$

$$\tilde{\mathbf{n}}_{\mathbf{c}}=-\nabla\tilde{c}_c-\tilde{c}_c\nabla\tilde{\phi}+\tilde{\mathbf{v}}\tilde{c}_cPe, \tag{4.14}$$

$$\tilde{\mathbf{n}_{\mathbf{a}}}=-\nabla\tilde{c}_a+\tilde{c}_a\nabla\tilde{\boldsymbol{\phi}}+\tilde{\mathbf{v}}\tilde{c}_a(M-Pe), \tag{4.15}$$

$$\tilde{c}_c=\tilde{c}_a, \tag{4.16}$$

$$\tilde{\mathbf{n}}_{\mathbf{a}}\cdot\tilde{\mathbf{n}}|_{\tilde{h}_c}=0, \tag{4.17}$$

$$\frac{\partial\tilde{h}_c}{\partial t}=\tilde{\mathbf{n}}_{\mathbf{c}}\cdot\tilde{\mathbf{n}}|_{\tilde{h}_c}, \tag{4.18}$$

where C_0 and V_0 are the average concentration and velocity, respectively.
The electrochemical energy of the cation at the metal boundary is

$$\Psi_c(X,\tilde{H}_c,T)=\Psi_c^0+RT_0\ln(\tilde{C}_c(X,\tilde{H}_c,T))+F\tilde{\Phi}(X,\tilde{H}_c,T), \tag{4.19}$$

where Ψ_c^0 is the standard electrochemical energy for the electrolyte, R is the universal gas constant, T_0 is the operating cell temperature. We assume fast kinetics, and neglect activation electrostatic potential, which is typically small for batteries [16]. The electrochemical energy in the metal electrode is

$$\Psi_m(X,T)=\Psi_m^0+\gamma v_mK(X,T)+F\tilde{\Phi}_m(X,T), \tag{4.20}$$

where γ is the surface tension at the electrode-electrolyte interface, Ψ_m^0 is the standard electrochemical energy for the electrode, K is the curvature, and $\Phi_m(X,T)$ is the electrostatic potential at the metal electrode surface.

Assuming equilibrium at the metal electrode surface gives

$$\tilde{\Phi}_m = \frac{\Psi_c^0 - \Psi_m^0}{F} + \frac{RT_0}{F}\ln(\tilde{C}_c(X,\tilde{H}_c,T)) - \frac{\gamma v_m K(X,T)}{F} + \tilde{\Phi}(X,\tilde{H}_c,T). \tag{4.21}$$

For charging the cell, an overpotenial

$$\tilde{E}_0 = \tilde{\Phi}(X,-L/2,T). \tag{4.22}$$

is applied at the counter -electrode. Substituting the non-dimensional variables $k = KL$, $\tilde{\phi}_m = F\tilde{\Phi}_m/(RT_0) - 6.91$, $\psi_c^0 = \Psi_c^0/(RT_0)$, $\beta = \gamma v_m/(RT_0 L)$, and $\psi_m^0 = \Psi_m^0/(RT_0)$, and $\tilde{e}_0 = \frac{\tilde{E}_0 F}{RT_0}$ we obtain the non-dimensional equations

$$\tilde{\phi}_m = \psi_c^0 - \psi_m^0 + \ln(\tilde{c_c}(x,\tilde{h_c},t)) - \beta k(x,t) + \tilde{\phi}(x,\tilde{h}_c,t), \tag{4.23}$$

and

$$\tilde{\phi}(x,-0.5,t) = \tilde{e}_0. \tag{4.24}$$

4.2 Base Case Solutions

For the base case, uniform plating and fully developed conditions are assumed, so $\tilde{J}(X,T) = J$, $\tilde{c}_c(x,z,t) = c_c(z)$, $\tilde{c}_a(x,z,t) = c_a(z)$, $\tilde{\phi}(x,z,t) = \phi(z)$, $\tilde{e}_0(x,z,t) = e_0$, $\tilde{\mathbf{v}}(x,z,t) = v(z)\hat{\mathbf{i}}$, and $\tilde{h}_c(x,t) = h_c(t)$, where J is the charging current density. J/F is the cation flux in the z direction, where F is Faraday's constant. The anion flux in the z direction is assumed to be zero. Substituting these expressions into Eqs. 4.14-4.18 and

Property	Value
C_0	$1\ M$
T_0	$300\ K$
L	$20\ \mu m$
D_a	$4E-10\ m^2s^{-1}$ [16]
D_c	$10^{-11}\ m^2s^{-1}$ [14]
F	$96500\ Cmol^{-1}$
R	$8.314\ Jmol^{-1}K^{-1}$
γ	$1.716\ Nm^{-1}$ [16]
μ_c	$D_c/(RT_0)\ mols^{-1}N^{-1}$
μ_a	$D_a/(RT_0)\ mols^{-1}N^{-1}$
v_m	$1.33E{-}5\ molm^{-3}$ [16]
μ	$4.152E-3\ Pas$
ρ	$1300\ kgm^{-3}$

Table 4.1. Parameters used in the model

4.24, setting $k = 0$ for the planar electrode in the base case, using the boundary conditions $c_a(z = -0.5) = c_{a0}$, and $\phi(z = 0.5) = 0$, and starting with the initial condition $h_c = 0.5$ gives the base case solutions

$$c_c = c_{a0} - j(z + 0.5)/2, \tag{4.25}$$

$$\phi = e_0 + ln\left(\frac{c_{a0} - j(z + 0.5)/2}{c_{a0}}\right), \tag{4.26}$$

$$c_{a0} = 1 + j/4, h_c = 0.5 - jt, e_0 = ln\left(\frac{1 + j/4}{1 - j/4}\right), \tag{4.27}$$

where $j = \frac{JL}{FD_cC_0}$.

Using a no slip boundary condition at the counter electrode gives

$$\tilde{v}(-0.5) = 0. \tag{4.28}$$

A no slip boundary condition at the metal electrode gives

$$\tilde{v}(\tilde{h_c}) = 0, \tag{4.29}$$

for Poiseuille flow and

$$\tilde{v}(\tilde{h_c}) = 2, \tag{4.30}$$

for Couette flow.

Using these boundary conditions leads us to the following solutions

$$v = 1.5 - 6z^2, \tag{4.31}$$

and

$$v = 2z + 1, \tag{4.32}$$

for Poiseuille and Couette flows. respectively.

Figures 4.2a, 4.2b, and 4.2c show the concentration, electrostatic potential, and electric field profiles at 2 different electrostatic potentials using the parameters for a lithium metal cell listed in Tab. 4.1. The base case solutions are independent of flow rate because the concentration and velocity profiles are assumed to be fully developed. While the concentration and electrostatic potential decrease from the positive electrode to the metal electrode, the electric field increases to its maximum at the negative electrode. Higher electrostatic potential implies higher current which requires higher electric field and concentration gradient [16]. The current density depends on applied electrostatic potential as shown in Fig. 4.3. As the applied electrostatic potential increases, current density also increases.

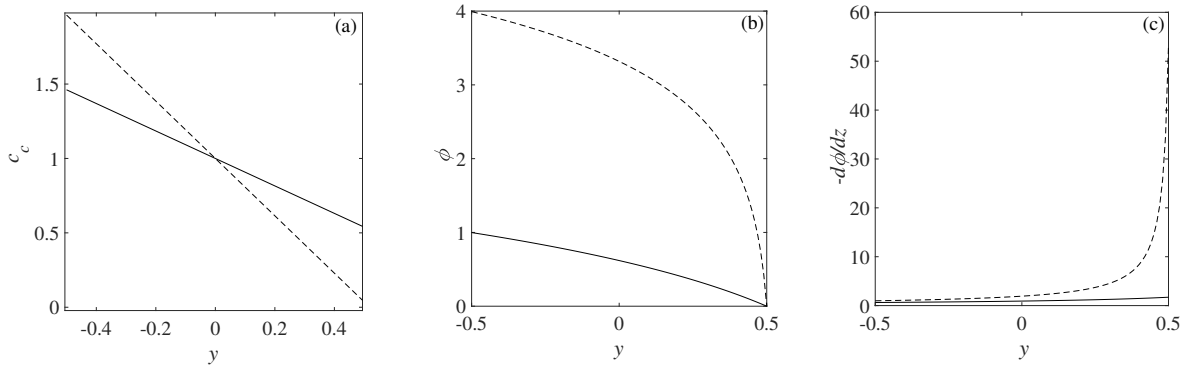

Figure 4.2. Base case solutions of non-dimensionalized (a) Concentration, (b) Electrostatic potential and (c) Electric field at $e_0 = 1$ (solid) and $e_0 = 4$ (dashed)

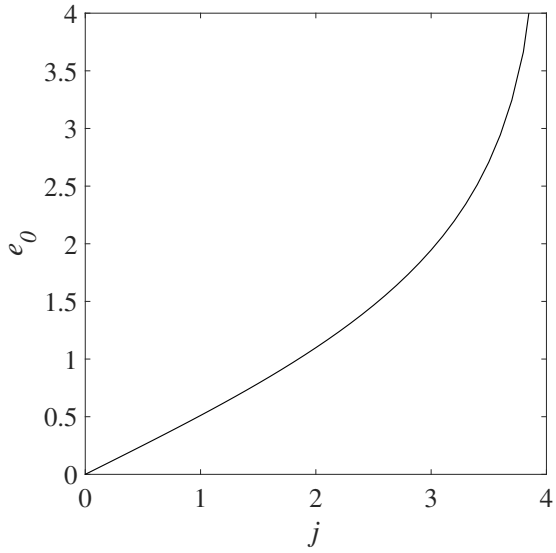

Figure 4.3. Electrostatic potential versus current

4.3 Stability analysis

To determine whether the flat deposition of the base case is stable, we perturb the metal surface with an infinitesimally small sinusoid

$$\tilde{h_c} = h_c + h_c' exp(\sigma t) exp(ikx), \tag{4.33}$$

where k, h'_c and σ are the non-dimensional wavenumber, non-dimensional amplitude, and non-dimensional exponential growth rate, respectively. The wavenumber equals $2\pi/\lambda$ where λ is the wavelength. The perturbations grow and decay exponentially fast for $\sigma > 0$ and $\sigma < 0$, respectively. Curvature of the perturbed surface concentrates the electric field lines and increases the ionic concentration gradient near the plating surface. Thus, plating on the perturbation tip is a function of curvature and wavenumber (k). We assume that no electrodeposition occurs on the positive electrode, so it is not perturbed.

We assume that concentration, electrostatic potential, and current density are also sinusoidally perturbed:

$$\tilde{c_c} = c_c + c'_c exp(\sigma t) exp(ikx), \tag{4.34}$$

$$\tilde{\phi} = \phi + \phi' exp(\sigma t) exp(ikx), \tag{4.35}$$

$$\tilde{j} = j + j' exp(\sigma t) exp(ikx), \tag{4.36}$$

where c'_c, ϕ', and j' are the non-dimensional perturbation amplitudes in cation concentration, electrostatic potential, and current density, respectively.
Perturbation analysis of Eq. 4.23 gives

$$\frac{c'_c(0.5)}{c_c(0.5)} + \frac{1}{c_c(0.5)}\frac{dc_c}{dz}(0.5)h'_c + \phi'(0.5) + \frac{d\phi}{dz}(0.5)h'_c = -\beta h'_c k^2. \tag{4.37}$$

In an infinitesimally small region very close to the lithium metal electrode surface, $v' = 0$, where v' is the normal component of velocity perturbation. So, the normal component of anion flux has only diffusion and migration terms. Substituting $v' = 0$ and subtracting

the base case from Eq. 4.17, and using electroneutrality gives $\phi' = \frac{c_c'}{c_c}$. This functional form is only valid in an infinitesimally small region close to the lithium metal electrode where $v' = 0$. Using this functional form for ϕ' yields

$$\phi'(0.5) = \frac{c_c'(0.5)}{c_c(0.5)} \tag{4.38}$$

The electrolyte velocity is perturbed according to

$$\tilde{\mathbf{v}} = v\hat{\mathbf{i}} + v'\hat{\mathbf{k}}exp(\sigma t)exp(ikx) + u'\hat{\mathbf{i}}exp(\sigma t)exp(ikx). \tag{4.39}$$

Pressure in the electrolyte will also have first order sinusoidal perturbations given by

$$\tilde{p} = p + p'exp(\sigma t)exp(ikx). \tag{4.40}$$

Substituting Eqs. 4.39, and 4.40 in Eqs. 4.12, and 4.13 gives

$$iku' + \frac{dv'}{dz} = 0, \tag{4.41}$$

$$-ikp' + Pe\left(\frac{d^2u'}{dz^2} - k^2u'\right) = 0, \tag{4.42}$$

$$-\frac{dp'}{dz} + Pe\left(\frac{d^2v'}{dz^2} - k^2v'\right) = 0. \tag{4.43}$$

No slip and no penetration at both electrodes provides boundary conditions

$$u'(-0.5) = 0, \tag{4.44}$$

$$v'(-0.5) = 0, \tag{4.45}$$

$$v'(0.5 + h_c') = 0. \tag{4.46}$$

For Couette flow,

$$u'(0.5 + h'_c) = -2h'_c \tag{4.47}$$

and for Poiseuille flow,

$$u'(0.5 + h'_c) = 6h'_c. \tag{4.48}$$

At the perturbed lithium metal electrode surface ($z = 0.5 + h'_c$), u' is non-zero to satisfy the no slip boundary conditions. This is because, as per the base case, $v(0.5) = 0$, but at the perturbed lithium metal electrode surface ($z = 0.5 + h'_c$), v is non-zero. Solving Eqs. 4.41-4.43, eliminating p' and using boundary conditions 4.44-4.46 gives u' and v'.

Eqs. 4.36 and 4.18 imply

$$\sigma h'_c = 2\frac{dc'_c}{dz}(0.5 + h'_c) - Mv'(0.5 + h'_c)c_c(0.5 + h'_c). \tag{4.49}$$

Solving Eqs. 4.41-4.43, and 4.49 using the boundary conditions 4.44-4.46 and 4.37 produces perturbation growth rate as a function of wavenumber.

Figures 4.4 and 4.5 show the variation of non-dimensional perturbation growth rate as a function of non-dimensional wavenumber at a given electrostatic potential and various flow rates in the creeping flow regime for Poiseuille and Couette flows, respectively.

For a fixed charging electrostatic potential and current density, perturbation growth rate attains a maximum with increasing wavenumber and then reduces. This is due to the competing effects of enhanced concentration gradient at dendrite tips and large energy required for electrodeposition on curved surfaces. For wavenumbers higher than a critical wavenumber, the perturbation growth rate is negative, indicating stable plating.

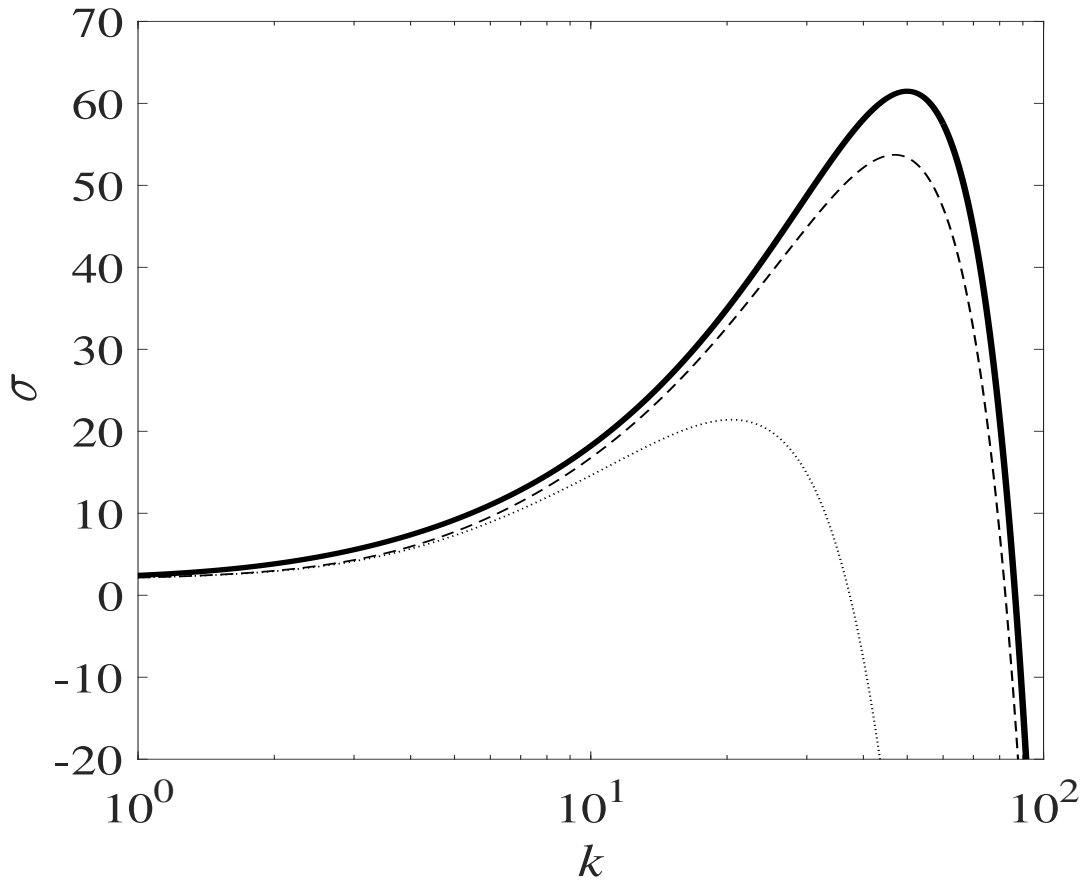

Figure 4.4. Poiseuille flow: Non-dimensional growth rate versus non-dimensional wavenumber at $e_0 = 1$, $Pe = 0$ (bold), $Pe = 3E3$ (dashed), $Pe = 3E4$ (dotted)

In the creeping flow regime, increasing the flow rate reduces the perturbation growth rate, the critical wavenumber, and the wavenumber at which maximum perturbation growth rate is obtained. The parallel flow rates are very high compared to the $Pe = 1$ flow required for stable, dendrite-free plating with uniform normal flow as described in chapter 2. This is expected because the stabilizing effect for normal flow with porous electrodes comes from the increased contribution of advective flux at the Li metal electrode in the base case (see chapter 2), whereas only the velocity perturbations contribute to stability in case of parallel flow. Also, unlike normal flows, creeping parallel flows cannot completely stabilize ($\sigma < 0$ for all $k > 0$) electrodeposition.

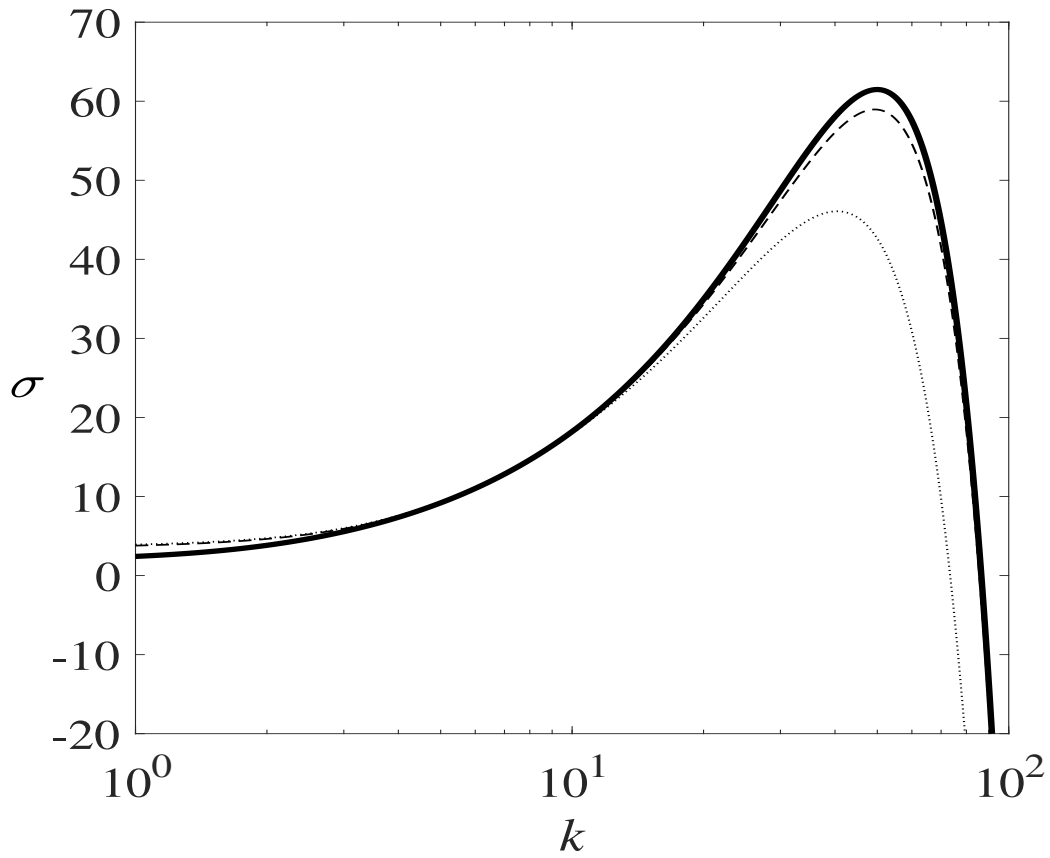

Figure 4.5. Couette flow: Non-dimensional growth rate versus non-dimensional wavenumber at $e_0 = 1$, $Pe = 0$ (bold), $Pe = 3E3$ (dashed), $Pe = 3E4$ (dotted)

Figure 4.6 shows the variation of σ with k for a fixed flow rate at two different charging electrostatic potentials for both Poiseuille and Couette flow. Higher charging electrostatic potentials implies higher charging current which leads to a larger dendrite growth rate. Fig. 4.4 shows that at both $e_0 = 2$ and $e_0 = 4$, Poiseuille flow stabilizes electrodeposition better than Couette flow. This possibly arises from the larger magnitude of u' at the metal electrode surface for Poiseuille flow than for Couette flow, as is evident from Eqs. 4.47 and 4.48. Although $v' = 0$ at the lithium metal electrode surface, for both Poiseuille and Couette flow, larger u' at the lithium metal electrode implies larger v' near the lithium metal electrode surface. The stabilizing effect of flow mainly arises from the normal velocity perturbations v', so larger v' near the lithium metal electrode

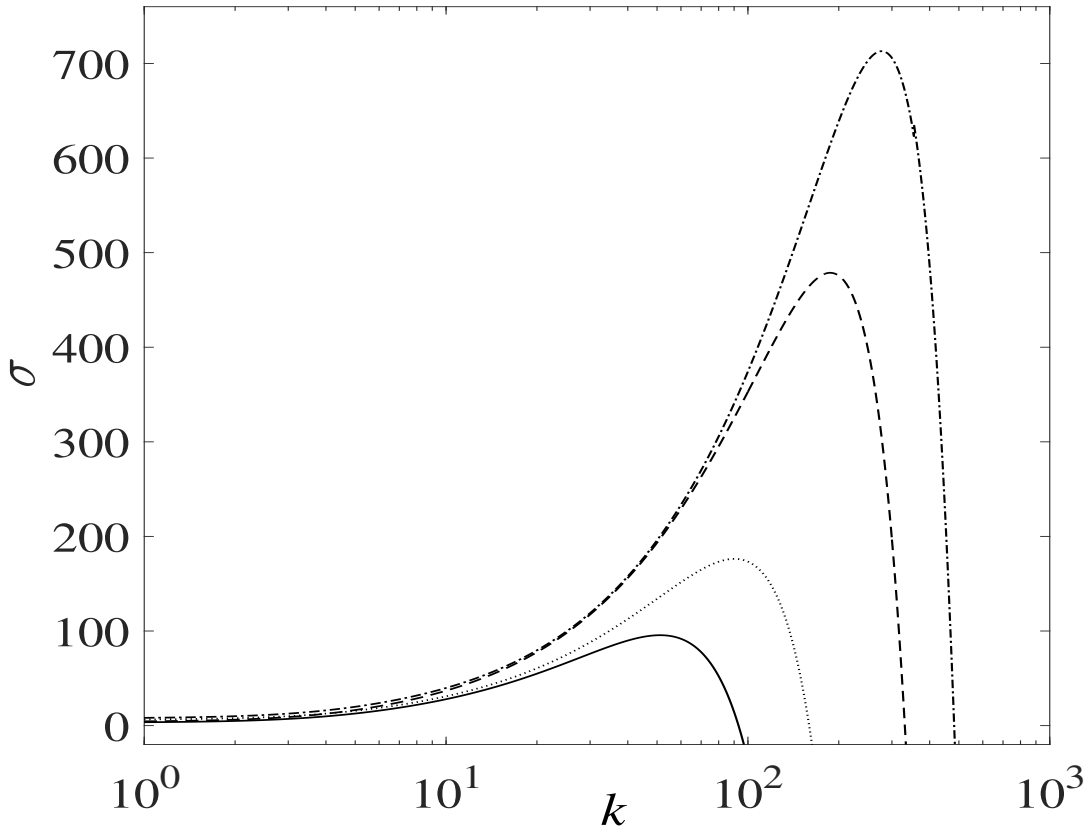

Figure 4.6. Non-dimensional growth rate versus non-dimensional wavenumber at $Pe = 3E4$, $e_0 = 2$ for Poiseuille flow (solid), $e_0 = 2$ for Couette flow (dotted), $e_0 = 4$ for Poiseuille flow (dashed), and $e_0 = 4$ for Couette flow (dashed-dotted).

surface for Poiseuille flow implies lesser perturbation growth rate.

4.4 Discussion

In chapters 2 and 3 have shown that normal flow towards a porous or perforated lithium metal electrode helps eliminate dendrites. Zheng *et al.* [88] experimentally show that dendrites in zinc electrodeposition on a rotating disk electrode can be eliminated at higher rotation rates. Thus, normal flow towards a non-porous metal electrode also can eliminate dendrites. This chapter, for the first time, shows that creeping Poiseuille and Couette flows parallel to the electrode can significantly reduce dendrite growth. Since,

electrolyte velocity can be represented by a combination of velocities normal and parallel to the metal electrode, creeping flow in general, helps stabilize or reduce the instabilities in plating. Increasing the flow rate beyond the creeping flow regime, however, may lead to increased dendrite growth as observed experimentally by Huang *et al.* [80].

We do not explicitly account for breakage and reformation of SEI. SEI breakage typically occurs due to large volume change associated with plating and stripping Li from under the SEI or excessive tensile stress at the dendrite tips. This can lead to inhomogeneities in the SEI layer, which can initiate dendrites. At the dendrite tips, SEI may fail under excessive tensile stress [2] which depends on curvature. For the sinusoidal perturbations that we consider in this study, the dendrite tip curvature is proportional to the amplitude and the square of the wavenumber. Parallel flows reduce the dendrite growth rate and shift maximum growth rate to smaller curvatures, so dendrite growth is slower and flatter, reducing the potential for SEI breakage.

Maraschky *et al.* [23] have shown that transport through the SEI layer is an important factor that can affect the onset of dendrite growth in lithium metal batteries. The thickness of SEI layer is often very small compared to the inter-electrode gap and hence any change of diffusion coefficient within the SEI layer would have a negligible effect. It is important to note that the linear stability analysis technique used in this chapter is similar to the techniques used for studying ramified deposits of zinc, copper, and silver that do not have SEI. The origin of dendrite growth in such metals is a electrohydrodynamic instability [118]. Moreover, zinc dendrites grow only at current densities larger than the limiting current density [88].

Typically pouch cells have a porous separator to electronically insulate the two electrodes

from each other and this will impede the proposed electrolyte flow and ionic diffusion. For both Poiseuille and Couette flow, ion diffusion would be slowed by the separator but this can be accommodated within the current model by reducing the diffusivity constant.

For Poiseuille flow, the presence of a porous separator increases the pressure required to pump the electrolyte through the inter-electrode gap but the flow profile is unchanged. For Couette flow, the flow profile depends on whether the separator is shearing or translating relative to one of the electrodes. For a porous separator that fills almost the entire gap, the velocity profile would be unchanged but the force required to move the electrode would increase. However, for a separator that is moving as a rigid body, the velocity profile would be different.

Chapter 5

Solid electrolyte interphase growth in lithium metal cells with normal electrolyte flow

SEI growth is an important feature of LMBs and is also related to the coulombic efficiency and cycle life of a battery. In this chapter, we study the effect of creeping normal flow on SEI growth in LMBs and further explore its effects on coulombic efficiency and cycle life.

5.1 Governing Equations

Figure 5.1 shows a schematic diagram of the Li metal cell with electrolyte flow normal to the lithium metal electrode. We assume that a charging current density J_{tot} leads to a flux $\mathbf{N_c}$ which transports Li^+ ions from the positive electrode at $Z = 0$ to the Li metal electrode at $Z = L$ where they may either plate or be consumed to generate SEI. We also assume the electrodes to be perforated or porous (*e.g.* metal foam) with sufficiently fine scaled pore structure to allow uniform normal electrolyte flow. The SEI layer on the porous electrodes is also assumed to be porous and much thinner than the

inter-electrode gap. Within the electrolyte (neglecting the double layer region)

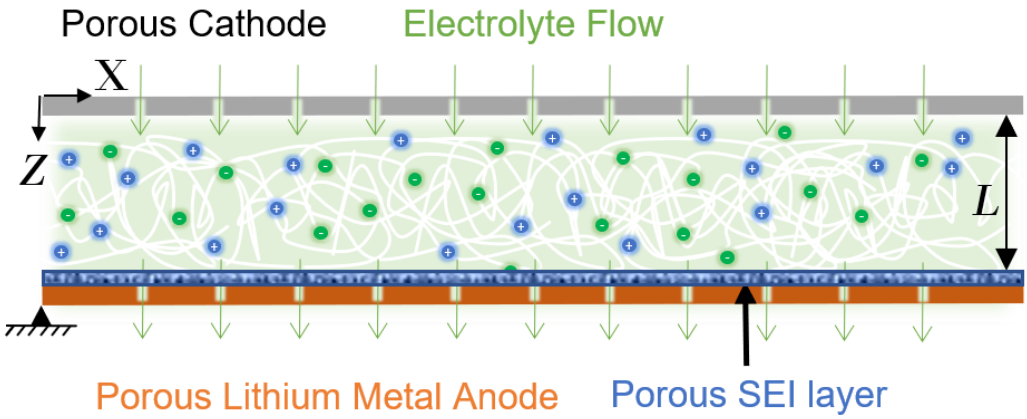

Figure 5.1. Schematic diagram of the lithium metal cell model with uniform normal electrolyte flow through porous Solid Electrolyte Interphase (SEI) layer and porous electrodes.

$$0 = -\nabla \cdot \mathbf{N_c}, \tag{5.1}$$

$$0 = D_c \frac{\partial^2 C_c}{\partial Z^2} + \mu_c F C_c \frac{\partial^2 \Phi}{\partial Z^2} + \mu_c F \frac{\partial C_c}{\partial Z}\frac{\partial \Phi}{\partial Z} - v\frac{\partial C_c}{\partial Z}, \tag{5.2}$$

$$0 = D_a \frac{\partial^2 C_a}{\partial Z^2} - \mu_a F C_a \frac{\partial^2 \Phi}{\partial Z^2} - \mu_a F \frac{\partial C_a}{\partial Z}\frac{\partial \Phi}{\partial Z} - v\frac{\partial C_a}{\partial Z}, \tag{5.3}$$

where F is Faraday's constant, D is diffusivity, μ is electric mobility, $\mathbf{N_c}$ is the solute flux, $C(Z)$ is solute (ion) concentration, $\mathbf{v} = v\hat{\mathbf{k}}$ is the electrolyte velocity, and $\Phi(Z)$ is electrostatic potential. The subscripts c and a indicate cation and anion respectively. Electroneutrality requires

$$C_c = C_a = C. \tag{5.4}$$

Using Eqs. 5.2-5.4 gives

$$0 = D\frac{\partial^2 C}{\partial Z^2} - v\frac{\partial C}{\partial Z}, \tag{5.5}$$

where $D = \frac{2D_cD_a}{D_c+D_a}$ is the ambipolar diffusivity. Comparing Eqs. 5.1 and 5.5 gives

$$\mathbf{N_c} = \left(-D\frac{\partial C}{\partial Z} + vC\right)\widehat{\mathbf{k}}. \tag{5.6}$$

Solvent transport is governed by

$$0 = -\nabla \cdot \mathbf{N_s}, \tag{5.7}$$

$$\mathbf{N_s} = \left(-D_s\frac{\partial C_s}{\partial Z} + vC_s\right)\widehat{\mathbf{k}} \tag{5.8}$$

where $\mathbf{N_s}$ is the solvent flux, C_s is the concentration of the solvent, and D_s is the solvent diffusivity. The total charging current density is divided between plating current density J_p and SEI formation current density J_{sei} , so

$$J_{tot} = J_{sei} + J_p, \tag{5.9}$$

where the current densities are given by the Butler-Volmer equations

$$J_p = F\mathbf{N_c}(L) \cdot \widehat{\mathbf{k}} \tag{5.10}$$

$$J_p = K_pC_c(L,T)^{1-\alpha}\left[exp\left(\frac{-\alpha FN_p}{RT_0}\right) - exp\left(\frac{\alpha FN_p}{RT_0}\right)\right] \tag{5.11}$$

and

$$J_{sei} = F\mathbf{N_s}(L) \cdot \widehat{\mathbf{k}} \tag{5.12}$$

$$J_{sei} = K_{sei}\left[C_c(L)C_s(L)\right]^{1-\alpha}\left[exp\left(\frac{-\alpha FN_{sei}}{RT_0}\right) - exp\left(\frac{\alpha FN_{sei}}{RT_0}\right)\right] \tag{5.13}$$

where N_p and N_{sei} are the activation overpotentials for plating and SEI formation, K_p and K_{sei} are the pre-exponential factors for plating and SEI formation, respectively, α is the symmetry factor, and T_0 is the temperature.

Property	Value
C_0	$1\ M$
C_{0s}	$4.5\ M$ [119]
T_0	$300\ K$
L	$50\ \mu m$
D_a	$4E-10\ m^2s^{-1}$ [16]
D_c	$10^{-11}\ m^2s^{-1}$ [14]
D_s	$10^{-9}\ m^2s^{-1}$
F	$96500\ Cmol^{-1}$
R	$8.314\ Jmol^{-1}K^{-1}$
μ_c	$D_c/(RT_0)\ mols^{-1}N^{-1}$
μ_a	$D_a/(RT_0)\ mols^{-1}N^{-1}$
α	0.5 [57]
K_p	$1.1E-2\ \ Am^{-2}mol^{-0.5}m^{1.5}$ [57]
K_{sei}	$2.5E-9/C_{0s}\ \ Am^{-2}mol^{-1}m^3$ [57]

Table 5.1. Model parameters

Non dimensional variables are defined as, $j_{tot} = \frac{J_{tot}L}{FD_cC_0}$, $d = \frac{D}{D_c}$, $d_s = \frac{D_s}{D_c}$, $Pe = \frac{vL}{D_c}$, $\phi = \frac{\Phi F}{RT_0}$, $c_c = \frac{C_c}{C_0}$, $c_a = \frac{C_a}{C_0}$, $c_s = \frac{C_s}{C_0}$, $z = \frac{Z}{L}$, $\mathbf{n_c} = \frac{\mathbf{N_c}L}{D_cC_0}$, $\mathbf{n_s} = \frac{\mathbf{N_s}L}{D_cC_0}$ $j_{sei} = \frac{J_{sei}L}{FD_cC_0}$, $j_p = \frac{J_pL}{FD_cC_0}$, $\eta_p = \frac{FN_p}{RT_0}$, $\eta_{sei} = \frac{FN_{sei}}{RT_0}$, $k_p = \frac{K_pL}{FD_cC_0^{0.5}}$, and $k_{sei} = \frac{K_{sei}L}{FD_c}$ where C_0 and C_{0s} are the average solute and solvent concentrations, respectively. Substituting these variables in Eqs. 5.5-5.13 produces

$$0 = \frac{\partial^2 c_c}{\partial z^2} + c_c\frac{\partial^2\phi}{\partial z^2} + \frac{\partial c_c}{\partial z}\frac{\partial\phi}{\partial z} - Pe\frac{\partial c_c}{\partial z} \tag{5.14}$$

$$0 = \frac{\partial^2 c_a}{\partial z^2} - c_a\frac{\partial^2\phi}{\partial z^2} - \frac{\partial c_a}{\partial z}\frac{\partial\phi}{\partial z} - Pe\frac{D_c}{D_a}\frac{\partial c_a}{\partial z} \tag{5.15}$$

$$c_c = c_a = c, \tag{5.16}$$

$$0 = d\frac{\partial^2 c}{\partial z^2} - Pe\frac{\partial c}{\partial z}, \tag{5.17}$$

$$\mathbf{n_c} = \left(-d\frac{\partial c}{\partial z} + Pec\right)\widehat{\mathbf{k}}, \tag{5.18}$$

$$0 = d_s\frac{\partial^2 c_s}{\partial z^2} - Pe\frac{\partial c}{\partial z}, \tag{5.19}$$

$$\mathbf{n_s} = \left(-d_s \frac{\partial c_s}{\partial z} + Pec_s\right) \widehat{\mathbf{k}}, \tag{5.20}$$

$$j_{tot} = j_p + j_{sei}, \tag{5.21}$$

$$j_p = k_p c_c(1)^{1-\alpha} \left[exp\left(-\alpha\eta_p\right) - exp\left((1-\alpha)\eta_p\right)\right], \tag{5.22}$$

$$j_{sei} = k_{sei} c_c(1)^{1-\alpha} c_s(1)^{1-\alpha} \left[exp\left(-\alpha\eta_{sei}\right) - exp\left((1-\alpha)\eta_{sei}\right)\right]. \tag{5.23}$$

The applied charging current density leads to a non-dimensional electrostatic potential

$$e_0 = \frac{E_0 F}{RT_0} = \phi(0). \tag{5.24}$$

where E_0 is the dimensional counter-electrode potential. We assume that the electrostatic potential at the lithium metal electrode is 0, so

$$\frac{RT}{F} ln(C_c(L)) + N_p = V_{neg} \tag{5.25}$$

or

$$6.909 + ln(c_c(1)) + \eta_p = v_{neg} \tag{5.26}$$

where $v_{neg} = V_{neg}F/(RT)$ is the non-dimensional potential at the negative electrode. The equilibrium potential for SEI formation is assumed to be 0.8 V [120]. So,

$$\eta_p + ln(c(1)) + 6.909 = \eta_{sei} + 0.8F/(RT_0). \tag{5.27}$$

The nondimensional model given by Eqs. 5.14-5.27 differs from those in chapters 2 and 3 in two important ways. The solvent transport (Eq. 5.19) and the SEI layer kinetics (Eq. 5.23) have been added.

We use Eqs. 5.18 and 5.20 as boundary conditions at both $z = 0$ and $z = 1$. Using

these boundary conditions, Eqs. 5.17, 5.19, 5.21-5.23 and 5.27 are solved analytically to produce

$$c = \frac{j_{tot}}{Pe} + \left[c_{a0} - \frac{j_{tot}}{Pe}\right] \exp(zPe/d), \tag{5.28}$$

$$c_{a0} = \frac{j_{tot}}{Pe} + \frac{[1 - \frac{j_{tot}}{Pe}][Pe/d]}{\exp(Pe/d) - 1}, \tag{5.29}$$

$$c_s = \frac{j_{sei}}{Pe} + \left[c_{sa0} - \frac{j_{sei}}{Pe}\right] \exp(zPe/d_s), \tag{5.30}$$

$$c_{sa0} = \frac{j_{sei}}{Pe} + \frac{[1 - \frac{j_{sei}}{Pe}][Pe/d_s]}{\exp(Pe/d_s) - 1}. \tag{5.31}$$

Solving Eqs. 5.14, 5.15, and 5.17 and substituting Eqs. **??-??** gives

$$(d-1)(3 + ln(c_c)) + d_1 \int_1^z \frac{dz}{c_c} + d_2 = \phi. \tag{5.32}$$

Numerical integration of Eq. 5.32 using the boundary conditions

$$\phi(1) = 0, \tag{5.33}$$

$$M\mathbf{n_c} \cdot \widehat{\mathbf{k}}(0) = -\frac{\partial c_c}{\partial z}(0) - c_c \frac{\partial \phi}{\partial z}(0) + Pec_c(0), \tag{5.34}$$

produces $\phi(z)$ where $M = 1 + D_c/D_a$.

5.2 Results

The critical Peclet number, Pe_{cr}, is defined as the Peclet number at which advective flux equals the total ionic flux at the negative electrode. Chapter 2 shows that at steady state, critical flow rate or $Pe = Pe_{cr}$ leads to an almost uniform concentration profile given by $c_c = 1$ and hence we use that to calculate Pe_{cr}.

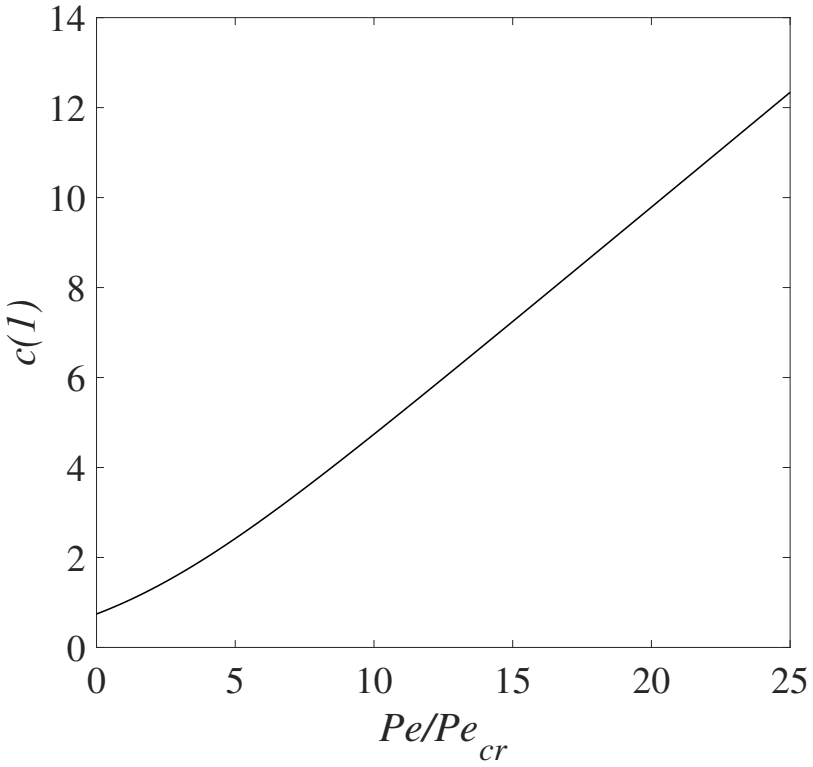

Figure 5.2. Electrolyte concentration at lithium metal electrode-electrolyte interface versus flow rate for $j = 1$.

Based on our previous results [121], we expect the concentration gradient and electrostatic potential gradient to reduce in magnitude with increasing flow rate and then the gradients change sign above the critical flow rate. Figs. 5.2 and 5.3 show that the electrolyte concentration at the lithium metal electrode surface and the electrostatic potential difference increase and decrease, respectively, with increasing flow rate. Based on Eqs. 5.28-5.31, the solvent concentration is expected to follow a similar pattern.

Assuming SEI layer formation and dead Li are the only Li sinks other than plating,

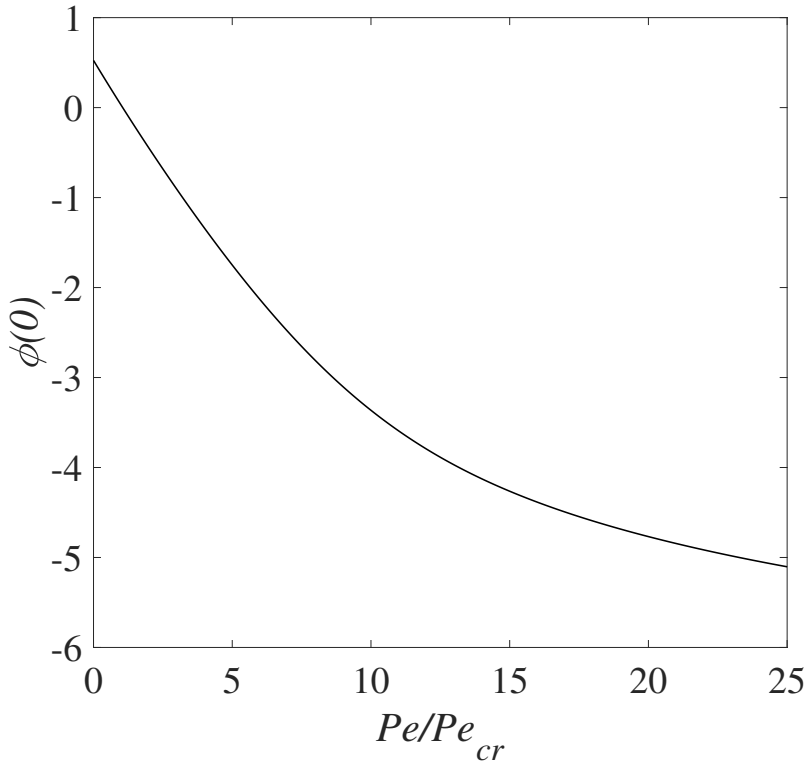

Figure 5.3. Charging electrostatic potential versus flow rate for $j = 1$.

coulombic efficiency (CE) can be defined as

$$CE = (DC/CC) = (1 - DL/CC - SEIC/CC), \tag{5.35}$$

where DC is discharge capacity, CC is charge capacity, $SEIC$ is the charge capacity lost in SEI formation, and DL is the amount of dead Li. As shown in chapter 2, flow rates above Pe_{cr} eliminate dendrites. So we assume that dead Li is eliminated under these conditions, and

$$CE = (DC/CC) = (1 - SEIC/CC) = j_p/j_{tot}. \tag{5.36}$$

Thus, increasing j_p/j_{tot} results in increased coulombic efficiency and cycle life. For typical charging current densities, Pe_{cr} is on the order of 1, so the dimensional critical

velocity is on the order of D_c/L. For $j = 1$ and parameters in Table 5.1, the critical velocity is on the order of $\mu m\ s^{-1}$. Thus, the required flow rates are very low and may be practically achieved using a variety of low power microfluidic pumping systems [122] along with porous or micropatterned electrodes [123–125].Programmed squeezing of a battery pack composed of pouch cells is another way to achieve the desired electrolyte flow.

Figure 5.4 shows that increasing the flow rate increases the j_p/j_{tot} ratio. At $Pe = 15Pe_{cr}$ and $j = 3$, coulombic efficiency of 99.3% is predicted. This is 6 % higher than without electrolyte flow and it corresponds to a 7X increase in cycle life. Figure 5.4 shows that at low flow rates (including $Pe = 0$), a high charging current density leads to a lower coulombic efficiency. This is similar to the observations in literature [47, 57]. Most models [51, 53, 57] in literature account for the SEI layer thickness evolution with time. We, however, assume the SEI layer thickness to be negligible with respect to the inter-electrode gap and hence do not account for the temporal evolution of its thickness. The model developed in this paper correctly predicts the reduction in coulombic efficiency with increasing current density at zero and low flow rates, thus indicating that our model is physically valid. At higher flow rates, the coulombic efficiencies flatten with respect to increasing charging current density and increasing flow rates. Under these conditions, lithium ions concentrate near the lithium metal electrode and increasing flow rate leads to a marginal increase in lithium ions available near the lithium metal electrode. Current literature values for coulombic efficiency in lithium metal cells mostly lie between 92% [79] - 99.1% [71]. Electrolyte flow accelerates both solvent and ion transport, so one might expect equal effects on both. Solvent diffusivity, however, is typically much higher than ionic diffusivity. Thus, ionic transport benefits more from advective transport leading to an increased CE due to an increase in j_p and reduction in j_{sei}.

The predicted CE values in Fig. 5.4 depends on the model parameters. We explore the sensitivity of CE to plating and SEI reaction constants. The nondimensional $k_p = 0.018$ and $K_{sei} = 1.93E-9$ from literature [57] are varied by a factor of 5 in both directions. Figures 5.5, 5.6, and 5.7 show the variation of j_p/j_{tot} with k_p and k_{sei} values. They show that a higher k_p and a lower k_{sei} imply low SEI growth rate for galvanostatic charging. This is probably because higher k_p values and lower k_{sei} values imply higher and lower reaction rates for plating and SEI formation, respectively. This is also evident from Eqs. 5.21-5.23. Moreover, a comparison of j_p/j_{tot} at same k_p and k_{sei} values indicates that a higher flow rate leads to higher coulombic efficiency. Finally, the top left corner of Fig. 5.7 shows coulombic efficiencies more than 99.9% $k_p \approx 0.1$ and $k_{sei} \approx$ 0.4E-9 with higher k_p values requiring higher k_{sei} values for the same coulombic efficiency. This may enable practical applications with about 225 cycles. These figures may be used as a guideline to tune the flow rate and electrolyte/solvent (rate constants) so as to obtain practical lithium metal batteries. A comparison of figures 5.5 and 5.7 shows that just tuning the electrolyte parameters within the explored ranges will not allow us to reach the high coulombic efficiency of 99.9%. It is necessary to tune the electrolyte/solvent and also use normal electrolyte flow to achieve high coulombic efficiencies.

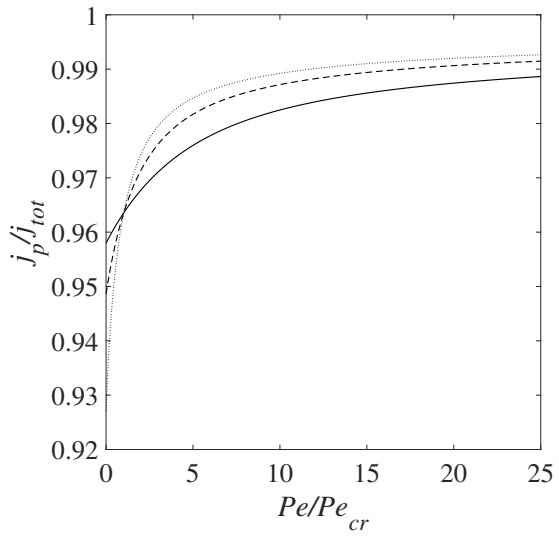

Figure 5.4. Ratio of plating current to total current at steady state versus Pe/Pe_{cr} for $j_{tot} = 1$ (solid), $j_{tot} = 2$ (dashed), $j_{tot} = 3$ (dotted).

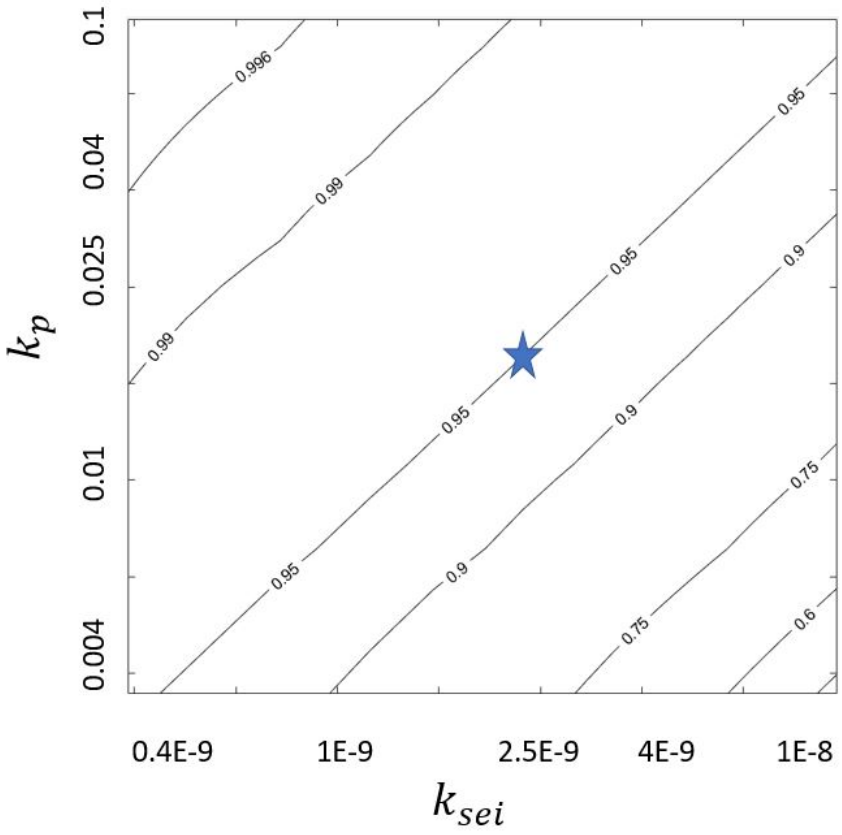

Figure 5.5. Variation of j_p/j_{tot} at $j_{tot} = 1$ and $Pe = 0$ with k_p and k_{sei} where 'star' indicates values chosen for Fig. 5.4.

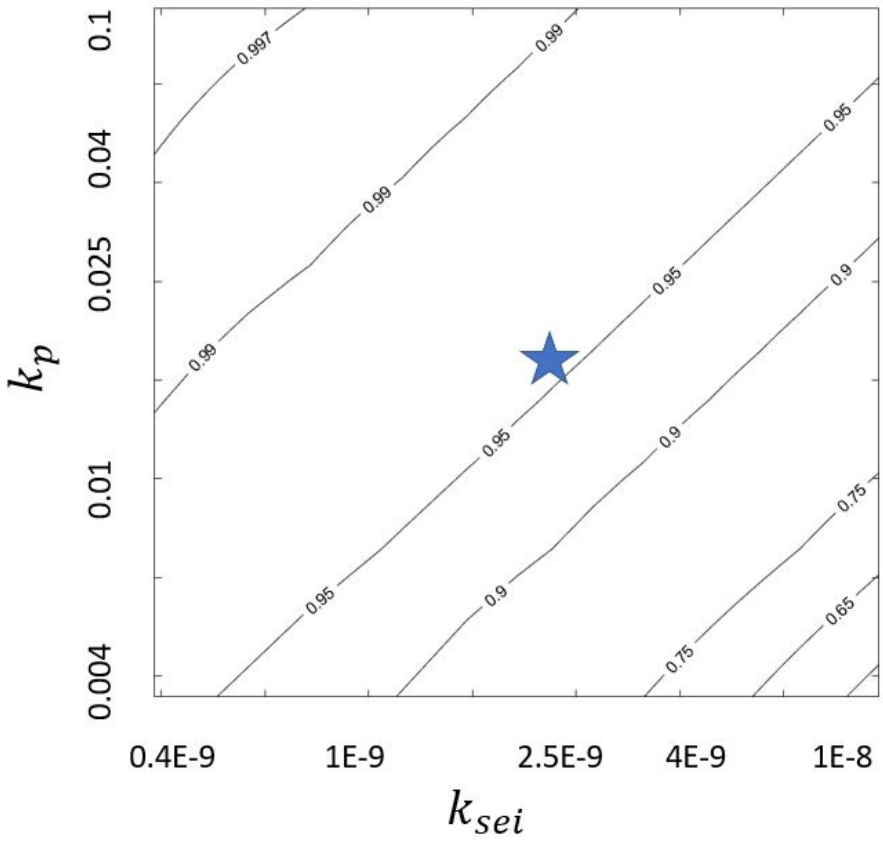

Figure 5.6. Variation of j_p/j_{tot} at $j_{tot} = 1$ and $Pe = Pe_{cr}$ with k_p and k_{sei} where 'star' indicates values chosen for Fig. 5.4.

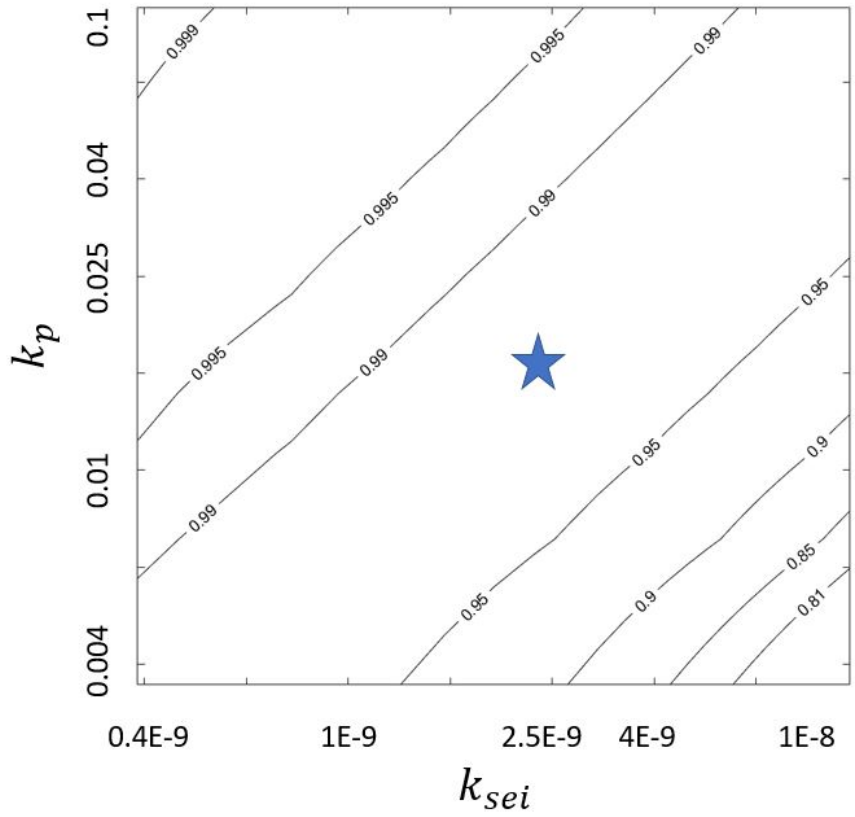

Figure 5.7. Variation of j_p/j_{tot} at $j_{tot} = 1$ and $Pe = 12.5Pe_{cr}$ with k_p and k_{sei} where 'star' indicates values chosen for Fig. 5.4.

Chapter 6

Normal electrolyte flow in zinc metal cells

This chapter studies the effect of creeping normal flow on zinc metal electrodeposition. The governing equations include transient terms that enable the prediction of the dynamic evolution of concentration and potential distributions. The possibility of dendrite growth is investigated through stability analysis and overlimiting current conditions.

6.1 Zinc electrochemistry

Figure 6.1 shows a symmetric zinc metal cell with zinc plated on a porous copper current collector for both electrodes. The aqueous zinc sulphate electrolyte is pumped through the positive electrode across the inter-electrode gap, and through the negative electrode. Zinc is stripped from the positive electrode producing Zn^{2+} ions that travel through the electrolyte and plate on the negative electrode surface. The Zn deposition morphology tends to be dendritic, especially under high current charging and/or overlimiting conditions where the concentration at the negative electrode drops to zero.

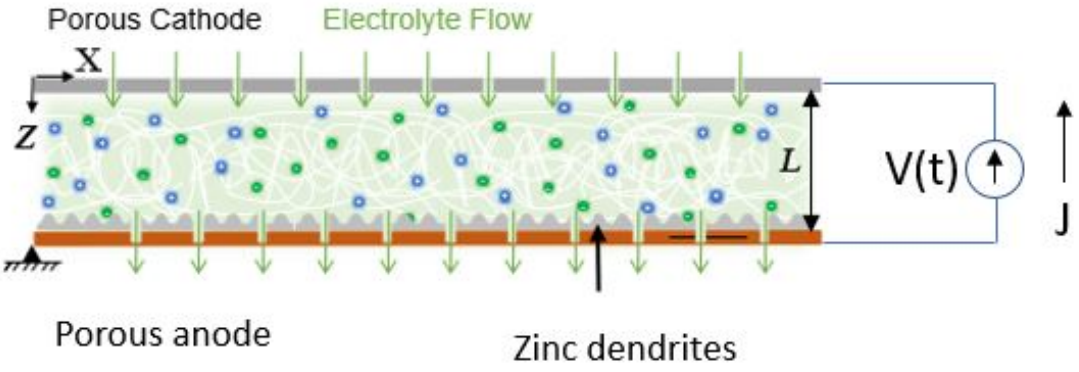

Figure 6.1. Schematic diagram of a symmetric zinc metal cell.

6.2 Governing Equations

Within the electrolyte of the zinc metal cell with uniform normal electrolyte flow through porous electrodes the time dependent governing equations are,

$$\frac{\partial C}{\partial T} = -\nabla \cdot \mathbf{N_c}, \tag{6.1}$$

$$\frac{\partial C_c}{\partial T} = D_c \frac{\partial^2 C_c}{\partial Z^2} + z_c \mu_c F C_c \frac{\partial^2 \Phi}{\partial Z^2} + z_c \mu_c F \frac{\partial C_c}{\partial Z}\frac{\partial \Phi}{\partial Z} - v\frac{\partial C_c}{\partial Z}, \tag{6.2}$$

$$\frac{\partial C_a}{\partial T} = D_a \frac{\partial^2 C_a}{\partial Z^2} - z_a \mu_a F C_a \frac{\partial^2 \Phi}{\partial Z^2} - z_a \mu_a F \frac{\partial C_a}{\partial Z}\frac{\partial \Phi}{\partial Z} - v\frac{\partial C_a}{\partial Z}, \tag{6.3}$$

where T is time, F is Faraday's constant, D is diffusivity, μ is electric mobility, $\mathbf{N_c}$ is the cation flux, $C(Z,T)$ is ion concentration, $\mathbf{v} = v\widehat{\mathbf{k}}$ is the electrolyte velocity, z is the valence of the ion, and $\Phi(Z,T)$ is electrostatic potential. The subscripts c and a indicate cation and anion respectively. The cation and anion diffusivities are calculated from the ambipolar diffusivity $D = \frac{2D_cD_a}{D_c+D_a}$, with $D_c/D_a = r_c/r_a$, where r_c and r_a are the radii of

hydrated cation and anion, respectively. With $z_c = z_a$, electroneutrality requires

$$C_c = C_a = C. \tag{6.4}$$

Using Eqs. 6.2-6.4 give

$$\frac{\partial C}{M\partial T} = D\frac{\partial^2 C}{\partial Z^2} - v\frac{\partial C}{\partial Z}, \tag{6.5}$$

$M = 1 + Dc/Da$. Comparing Eqs. 6.1 and 6.5 gives

$$\frac{\mathbf{N_c}}{M} = \left(-D\frac{\partial C}{\partial Z} + vC\right)\widehat{\mathbf{k}}, \tag{6.6}$$

$$\mathbf{N_c} = \left(-Dc\frac{\partial C_c}{\partial Z} + vC_c - \mu_c z_c \frac{F}{RT_0} C_c \frac{d\Phi}{dZ}\right)\widehat{\mathbf{k}}, \tag{6.7}$$

$$\mathbf{N_a} = \left(-Da\frac{\partial C_a}{\partial Z} + vC_a + \mu_a z_a \frac{F}{RT_0} C_a \frac{d\Phi}{dZ}\right)\widehat{\mathbf{k}}, \tag{6.8}$$

where $\mathbf{N_a}$ is the anion flux, T_0 is the operating cell temperature, and R is the universal gas constant. At steady state

$$N_c = \frac{J}{z_c F} \tag{6.9}$$

and

$$N_a = 0. \tag{6.10}$$

Non dimensional variables are defined as, $d = \frac{D}{D_c}$, $Pe = \frac{vL}{D_c}$, $\phi = \frac{\Phi F}{RT_0}$, $c_c = \frac{C_c}{C_0}$, $c_a = \frac{C_a}{C_0}$, $z = \frac{Z}{L}$, $\mathbf{n_c} = \frac{\mathbf{N_c}L}{D_c C_0}$, $c_{a0m} = \frac{C_{a0m}}{C_0}$, $c_{cL} = \frac{C_{cL}}{C_0}$, $j = \frac{JL}{z_c F D_c C_0}$, and $t = \frac{D_c T}{L^2}$, where C_0 is the average electrolyte concentration, C_{a0m} is the concentration at the positive electrode, and C_{cL} is the concentration at the negative electrode. Substituting these variables in

Property	Value
C_0	1 M
T_0	300 K
L	1 mm
D	$7.47E-10$ m^2s^{-1} [126]
D_a	$6.34E-10$ m^2s^{-1}
D_c	$9.09E-10$ m^2s^{-1}
F	96500 $Cmol^{-1}$
R	8.314 $Jmol^{-1}K^{-1}$
μ_c	$D_c/(RT_0)$ $mols^{-1}N^{-1}$
μ_a	$D_a/(RT_0)$ $mols^{-1}N^{-1}$
z_c	2
z_a	2
r_c	0.43 nm [127]
r_a	0.3 nm [128]
γ	0.575 Jm^{-2} [129]
v_m	0.916E-5 m^3mol^{-1} [130]

Table 6.1. Model parameters

Eqs. 6.2-6.10 produces

$$\frac{\partial c_c}{\partial t} = \frac{\partial^2 c_c}{\partial z^2} + z_c c_c \frac{\partial^2 \phi}{\partial z^2} + z_c \frac{\partial c_c}{\partial z}\frac{\partial \phi}{\partial z} - Pe\frac{\partial c_c}{\partial z} \tag{6.11}$$

$$(M-1)\frac{\partial c_a}{\partial t} = \frac{\partial^2 c_a}{\partial z^2} - z_a c_a \frac{\partial^2 \phi}{\partial z^2} - z_a \frac{\partial c_a}{\partial z}\frac{\partial \phi}{\partial z} - Pe(M-1)\frac{\partial c_a}{\partial z} \tag{6.12}$$

$$c_c = c_a = c, \tag{6.13}$$

$$\frac{\partial c}{\partial t} = \frac{2}{M}\frac{\partial^2 c}{\partial z^2} - Pe\frac{\partial c}{\partial z}, \tag{6.14}$$

$$\frac{\mathbf{n_c}}{M} = \left(-\frac{2}{M}\frac{\partial c}{\partial z} + Pec\right)\widehat{\mathbf{k}}, \tag{6.15}$$

$$\mathbf{n_c} = \left(-\frac{\partial c_c}{\partial z} + Pec_c - z_c c_c \frac{d\phi}{dz}\right)\widehat{\mathbf{k}}, \tag{6.16}$$

$$\mathbf{n_a} = \left(-\frac{\partial c_a}{\partial z} + Pec_c + z_a c_a \frac{d\phi}{dz}\right)\widehat{\mathbf{k}}. \tag{6.17}$$

At steady state

$$n_c = \frac{j}{F}, \tag{6.18}$$

$$n_a = 0. \tag{6.19}$$

The applied charging current density leads to a non-dimensional electrostatic potential

$$e_0 = \frac{E_0 F}{RT_0} = \phi(0, T), \tag{6.20}$$

where E_0 is the dimensional counter-electrode potential.

The electrochemical energy of the cation at the Zn metal boundary is

$$\Psi_c = \Psi_c^0 + RT_0 \ln(C_c) + z_c F \Phi \tag{6.21}$$

where Ψ_c^0 is the standard electrochemical energy for the electrolyte and the electrochemical energy in the Zn metal electrode is

$$\Psi_m = \Psi_m^0 + \gamma v_m K + z_c F \Phi_m, \tag{6.22}$$

where γ is the surface energy, K is the electrode surface curvature, Φ_m is the electrostatic potential of the Zn metal electrode surface, and Ψ_m^0 is the standard electrochemical energy for the electrode.

Assuming equilibrium at the metal electrode-electrolyte interface gives $\Psi_c = \Psi_m$, so

$$\Phi_m = \frac{\Psi_c^0 - \Psi_m^0}{z_c F} + \frac{RT_0}{z_c F} \ln(C_c) - \frac{\gamma v_m K}{z_c F} + \tilde{\Phi} \tag{6.23}$$

Non-dimensionalizing Eqs. 6.23 and 6.22 leads us to

$$z_c\phi_m = \psi_c^0 - \psi_m^0 + \ln(c_c) - \beta k + z_c\phi, \tag{6.24}$$

where $k = KL$, $\beta = \gamma v_m/(RT_0L)$, $\phi_m = F\Phi_m/(RT_0)$, $\psi_m^0 = \Psi_m^0/(RT_0)$, and $\psi_c^0 = \Psi_c^0/(RT_0)$. The initial condition is uniform concentration for the electrolyte. The nondimensional model given by Eqs. 6.11- 6.16 differs from those in chapters 2 and 4 because diffusion time dependence has been included in (Eq. 6.14) to allow transient solutions.

We use Eq. 6.16 as boundary condition at both $z = 0$ and $z = 1$. Using these boundary conditions and initial condition $c = 1$, we obtain the analytical solutions for a step input $j(t) = j$

$$c_{ss} = \frac{j}{MPe} + \left[c_{a0m} - \frac{j}{MPe}\right]\exp(zPeM/2), \tag{6.25}$$

$$c = c_{ss} + \sum_{n=1}^{\infty} a_n exp(PezM/(2) - k_n t)(sin(\beta_n z) + 2\frac{2\beta_n}{MPe}cos(\beta_n z)) \tag{6.26}$$

$$c_{a0m} = \frac{j}{MPe} + \frac{[1 - \frac{j}{MPe}][MPe/2]}{\exp(MPe/2) - 1}, \tag{6.27}$$

$$a_n = \frac{\int_0^1 (1 - c_{ss})(exp(-MPez/(4)))(sin(\beta_n z) + 2\frac{2\beta_n}{MPe}cos(\beta_n z))dz}{\int_0^1 (sin\beta_n z) + 2\frac{2\beta_n}{MPe}cos(\beta_n z))^2 dz} \tag{6.28}$$

where $\beta_n = n\pi$ and $k_n = \beta_n^2 + (\frac{MPe}{4})^2$. The concentration distribution in Eq. 6.26 is sum of the steady state solution and the transient response. The coefficients a_n are obtained via orthogonality. Solving Eqs. 6.11, 6.12, and 6.14 and substituting Eqs. 6.25-6.28 gives

$$\left[\frac{2}{M} - 1\right](3 + ln(c_c)) + d_1\int_1^z \frac{dz}{c_c} + d_2 = z_c\phi. \tag{6.29}$$

Numerical integration of Eq. 6.29 using the boundary conditions

$$\phi(1,t) = 0, \tag{6.30}$$

$$\mathbf{n_c} \cdot \widehat{\mathbf{k}}(0,t) = -\frac{\partial c_c}{\partial z}(0,t) - z_c c_c \frac{\partial \phi}{\partial z}(0,t) + Pe c_c(0,t), \tag{6.31}$$

produces $\phi(z,t)$. The nondimensional voltage V_0 required for charging is given by

$$z_c V_0 = log\left[\frac{c(0,t)}{c(1,t)}\right] + z_c\phi(0,t) \tag{6.32}$$

where the first term on RHS is the negative of the Nernst potential for the cell. The steady state solution ϕ_{ss} is given by

$$z_c\phi_{ss} = z_c e_0 + \ln\left[\frac{(c_{a0m} - \frac{j}{MPe})\exp(\frac{(2Pe-MPe)z}{2}) + \frac{j}{MPe}\exp((-MPe+Pe)z)}{c_{a0m}}\right]. \tag{6.33}$$

6.3 Transient analysis

Critical Pe (Pe_{cr}) is defined as the flow rate at which advective flux is equal to the total flux at the zinc metal anode. Figures 6.2 and 6.3 show the transient evolution of concentration and electrostatic potential distributions at $Pe = 0$ and $Pe = 2Pe_{cr}$, respectively. The initial concentration is uniform and converges to a steady state profile after a nondimensional time close to $t = 1$. The baseline case without flow in Fig. 6.2 shows the concentration growing at the cathode and reducing at the anode. If the current is high enough, the concentration at the anode will go to zero. Charging currents greater than this limiting current are thought to cause dendrite growth. Dendrites can lead to isolated Zn (dead Zn) that disconnects from anode, reducing active material and cycle life. Fig. 6.3 shows that flow drastically changes the concentration and electrostatic potential distributions. In Fig. 6.3, flow rate ($Pe = 2Pe_{cr}$) is greater than the

critical flow rate. In Fig. 6.3 concentration decreases at the cathode and increases at the anode. Thus, the chances of reaching overlimiting currents are greatly reduced.

Fig. 6.2 shows the electrostatic potential decreasing in time for the baseline case. The voltage jumps from 0 to 0.15 due to polarization impedance of the electrolyte and then increases as the concentration profile changes. With $Pe = 2Pe_{cr}$ in Fig. 6.3, the cathode potential jumps to 0.15 at t=0_+, and then increases due to the concentration profile changes. This means that steady state electrostatic potential is higher at $2Pe_{cr}$ than at $Pe = 0$, which is unlike what is observed in case of lithium. This is because $Dc/Da > 1$ for Zn and $Dc/Da < 1$ for Li.

Figure 6.4 shows the nondimensional voltage in response to step input $j = 0.5$ for different flow rates. The voltage goes from zero to 0.15 when the step input commences and the transient response goes up or down for flow rates below or above the critical flow rate. The response settles to steady state at t≈1, fairly independent of the flow rate. In dimensional units the settling time $\approx L^2/D_c = 1.1E3s$ for a 1 mm inter-electrode gap.

Figure 6.5 shows the steady state potential difference between the two electrodes versus flow rate for $j = 0.5$ and $j = 1$. For the cases considered in Fig. 6.5, increasing the flow rate reduces the charging voltage.

6.4 Stability analysis

The growth rate of the Zn metal electrode per unit surface area due to electrodeposition is given by

$$\frac{\partial \tilde{H}_c}{\partial T} = \left(\frac{v_m}{z_c F} \tilde{\mathbf{J}} \cdot \tilde{\mathbf{n}} \right) |_{\tilde{H}_c}, \tag{6.34}$$

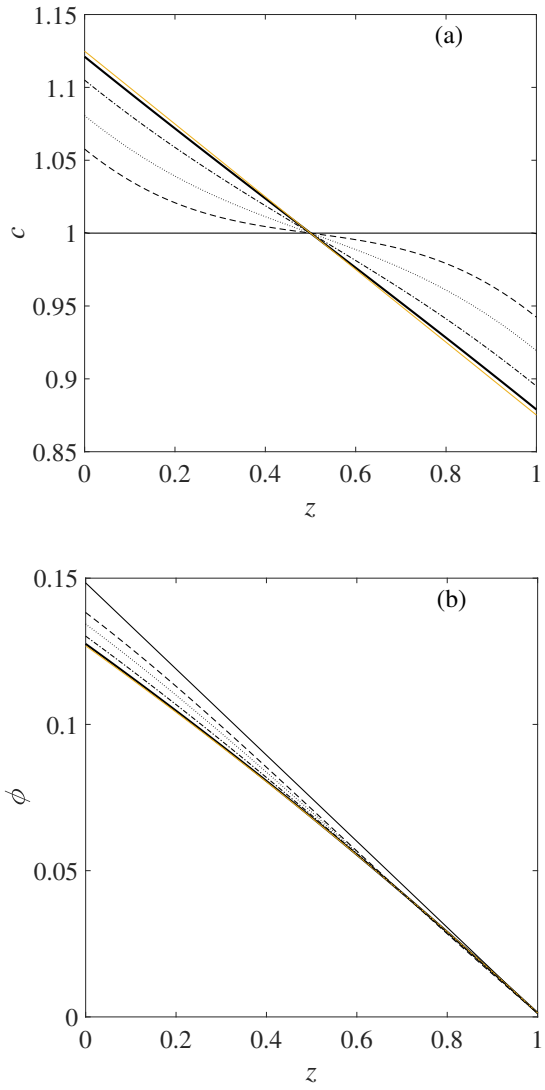

Figure 6.2. Nondimensional (a) concentration and (b) electrostatic potential profiles for $Pe = 0$ solid, $j = 0.5$ at $t = 0$ (solid), $= 0.05$ (dashed), $t = 0.1$ (dotted), $t = 0.2$ (dashed-dotted), $t = 0.4$ (bold), $t = 0.8$ (yellow).

where $\tilde{H}_c$ is the distance between zinc metal electrode and the positive electrode, v_m is the molar volume of Zn, and $()|_{\tilde{H}_c}$ means evaluated at the growing surface $\tilde{H}_c$. Nondimensionalizing the above equation gives

$$\frac{\partial \tilde{h_c}}{\partial t_1} = \tilde{\mathbf{j}} \cdot \tilde{\mathbf{n}}|_{\tilde{h_c}}, \tag{6.35}$$

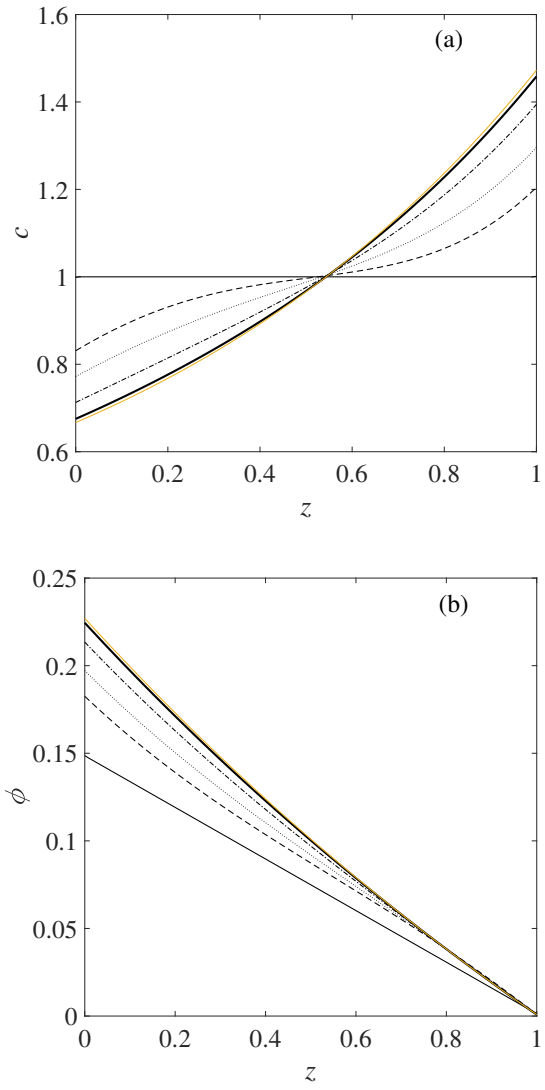

Figure 6.3. Nondimensional (a) concentration and (b) electrostatic potential profiles for $Pe = 2Pe_{cr}$ solid, $j = 0.5$ at $t = 0$ (solid), $= 0.05$ (dashed), $t = 0.1$ (dotted), $t = 0.2$ (dashed-dotted), $t = 0.4$ (bold), $t = 0.8$ (yellow).

where $t_1 = \frac{v_m D_c C_0 T}{L^2}$ and $\tilde{h_c} = \frac{\tilde{H_c}}{L}$.

We treat the steady state solutions as the base case and for stability analysis we introduce infinitesimally small sinusoidal perturbations given by

$$\tilde{h_c} = h_c + h_c' exp(\sigma t) exp(ikx), \tag{6.36}$$

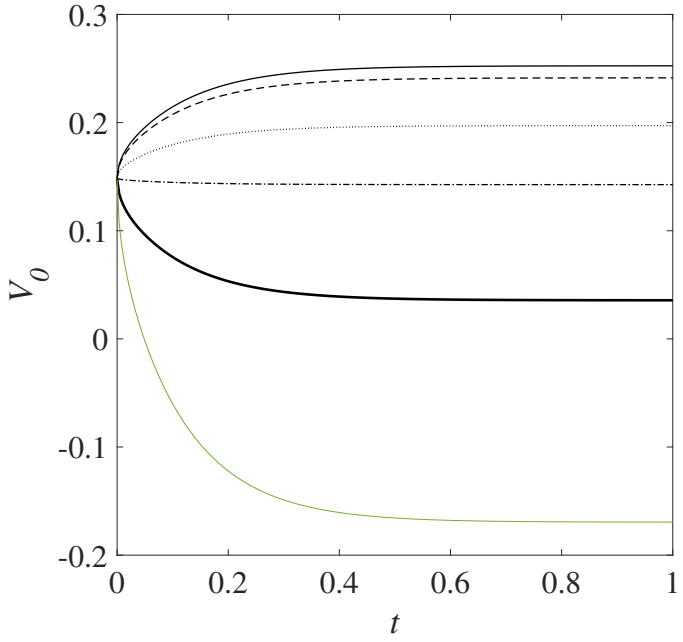

Figure 6.4. Nondimensional potential difference versus time for $j = 0.5$ at $Pe = 0$ (solid), $Pe = 0.05Pe_{cr}$ (dashed), $Pe = 0.25Pe_{cr}$ (dotted), $Pe = 0.5Pe_{cr}$ (dashed-dotted), $Pe = Pe_{cr}$ (bold), and $Pe = 2Pe_{cr}$ (green).

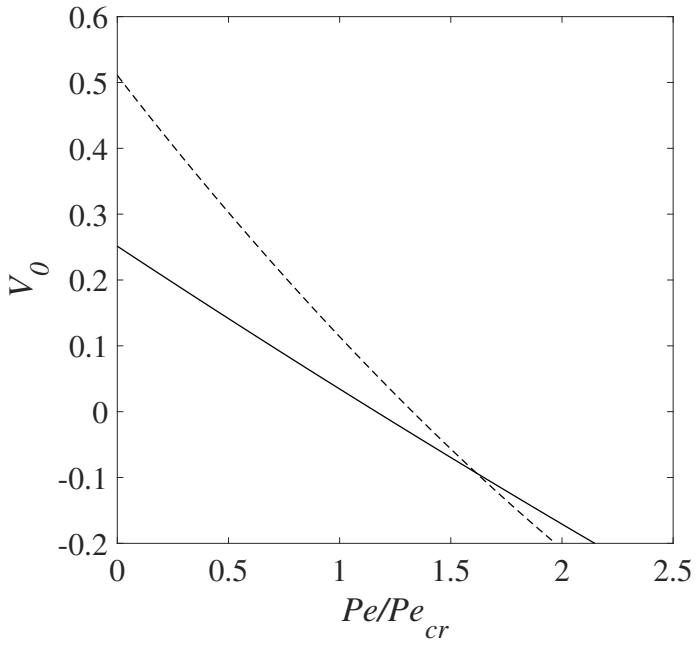

Figure 6.5. Nondimensional potential difference versus ratio between flow rate and critical flow rate for $j = 0.5$ (solid) and $j = 1$ (dashed).

where k, h_c' and σ are the nondimensional wavenumber, nondimensional amplitude, and nondimensional exponential growth rate on the negative electrode surface. These perturbations represent the inherent surface roughness or nucleated dendrites. The wavenumber equals $2\pi/\lambda$ where λ is the wavelength. So, the perturbation growth rate σ represents dendrite growth rate. σ greater than 0 indicates exponentially fast growing dendrites and σ less than 0 for all k implies stable plating. Growth rate σ depends on wavenumber k as dendrites with different curvatures may grow with different rates due to the effect of surface tension, varying concentration of electric field lines, and varying concentration gradient on the curved dendrite tips. We do not perturb the positive electrode surface as we do not expect any dendrites to grow on the positive electrode.

The introduction of surface perturbations on the negative electrode leads to concentration, electrostatic potential, and current density perturbations with similar spatial and temporal characteristics. They are given by

$$\tilde{c}_{ss} = c_{ss} + c'_{ss} exp(\sigma t_1) exp(ikx), \tag{6.37}$$

$$\tilde{\phi}_{ss} = \phi_{ss} + \phi'_{ss} exp(\sigma t_1) exp(ikx), \tag{6.38}$$

$$\tilde{\mathbf{j}} = j\hat{\mathbf{k}} + \mathbf{j}' exp(\sigma t_1) exp(ikx), \tag{6.39}$$

where c'_{ss}, ϕ'_{ss}, and j' are the non-dimensional amplitudes of the perturbations in cation concentration, electrostatic potential, and current density, respectively.

Substitution of Eqs. 6.37-6.39 into steady state versions of governing equations yields

$$\phi'_{ss} = z_c \frac{c'_{ss}}{c_{ss}}. \tag{6.40}$$

Eqs. 6.39 and Eq. 6.35 imply

$$\sigma h'_c = 2\frac{dc'_{ss}}{dz}(1) - MPec'_{ss}. \tag{6.41}$$

Eqs. 6.21, 6.22 give

$$\frac{c'_{ss}(1)}{c_{ss}(1)} + \frac{1}{c_{ss}(1)}\frac{dc_{ss}}{dz}(1)h'_c + z_c\phi'_{ss}(1) + z_c\frac{d\phi}{dz}(1)h'_c = -\beta h'_c k^2. \tag{6.42}$$

Solving the above equations leads to the following solution for the perturbation growth rate σ

$$\sigma = \frac{c_{ss}(1)}{2}\left[\frac{-1}{c_{ss}(1)}\frac{dc_{ss}}{dz}(1) - z_c\frac{d\phi_{ss}}{dz}(1) - \beta k^2\right]\left[2\frac{m_1 exp(m_1) - m_2 exp(m_2)}{exp(m_1) - exp(m_2)} - MPe\right], \tag{6.43}$$

where $m_1 = \frac{MPe+\sqrt{M^2Pe^2+16k^2}}{4}$ and $m_2 = \frac{MPe-\sqrt{M^2Pe^2+16k^2}}{4}$.

Critical wavenumber,

$$k_{cr} = \sqrt{\frac{1}{\beta}\left[\frac{-1}{c_{ss}(1)}\frac{dc_{ss}}{dz}(1) - z_c\frac{d\phi_{ss}}{dz}(1)\right]}, \tag{6.44}$$

is the wavenumber above which $\sigma < 0$. It maybe used as a measure of feature width for zinc plating.

Figure 6.6 shows that increasing the flow rate towards the negative zinc metal electrode reduces the maximum perturbation growth rate and the critical wavenumber. Higher

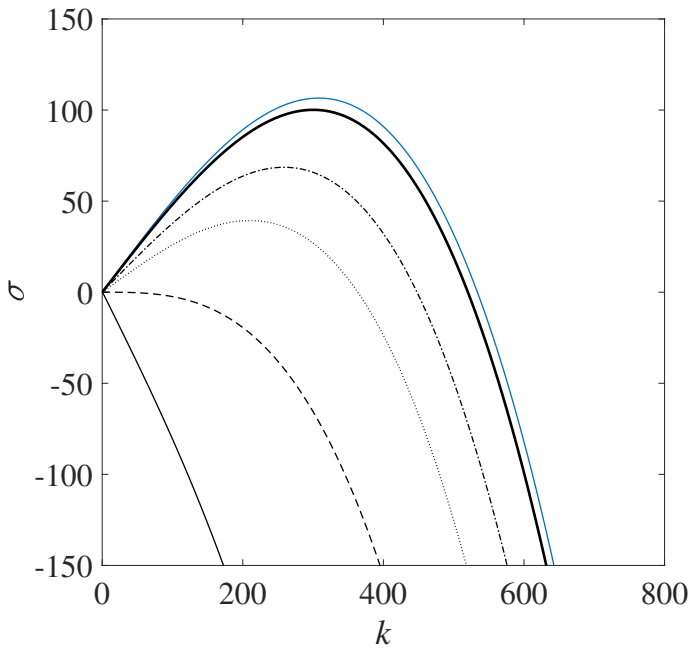

Figure 6.6. Nondimensional perturbation growth rate versus nondimensional wavenumber for $j = 0.5$ at $Pe = -0.05Pe_{cr}$ (blue), $Pe = 0$ (bold), $Pe = 0.25Pe_{cr}$ (dashed-dotted), $Pe = 0.5Pe_{cr}$ (dotted), $Pe = Pe_{cr}$ (dashed), and $Pe = 2Pe_{cr}$ (solid).

flow rate towards the negative zinc metal electrode lowers the dendrite growth rate and results in relatively flat deposits that are less likely to shed active material or cause internal shorting. Above the critical flow rate, the maximum perturbation growth rate is negative, so $Pe > Pe_{cr}$ is a good indicator of dendrite elimination.

Above the solid line in Fig. 6.7, the stability analysis predicts that dendrites will not grow. Above the dashed line in Fig. 6.7, the steady state analysis predicts Zn^{2+} concentration will be positive. Thus, increasing electrolyte flow rate reduces two key indicators of dendrite growth, increasing the cyclability and safety of Zn metal cells. Using the steady state result at low current densities, we calculate the volume of pumped electrolyte to be 18.65 ml/Ah.

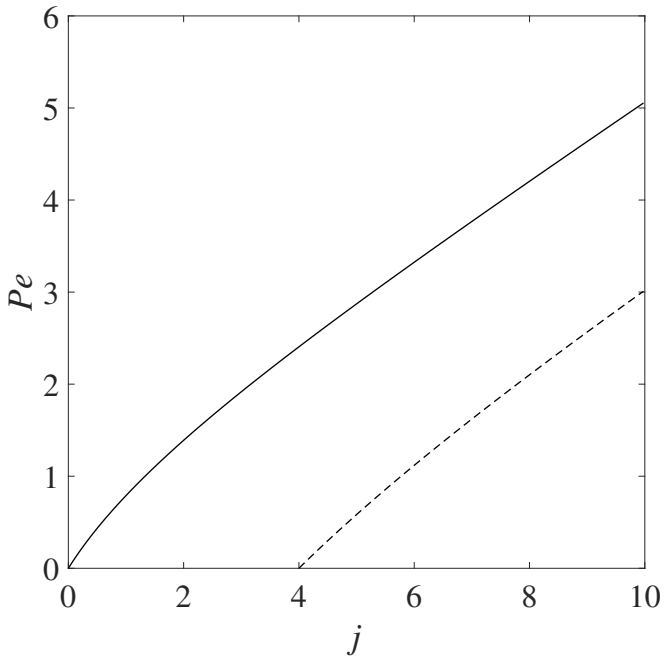

Figure 6.7. Critical Peclet number (solid) and minimum Peclet number required to prevent concentration depletion at negative electrode (dashed) versus nondimensional current density

Chapter 7
Conclusions

Chapter 2 shows that electrolyte flow towards the Li metal electrode lowers the dendrite growth rate, reduces the required overpotential, and reduces the impedance. Flow in the opposite direction, however, enhances the dendrite growth. For every current density, there exists a critical velocity above which dendrite growth can be totally eliminated. As shown in Fig. 2.4, the critical velocity increases almost linearly with increasing current density. For typical current densities and inter-electrode separation, the critical velocity is very small, indicating the potential for practical application. Supercritical flow is very small and could be achieved by several possible mechanisms, including microfluidic pumping systems [122] along with porous or micropatterned electrodes [123–125]. It may also be achieved by programmed squeezing deformations of a battery pack composed of pouch cells.

Chapter 3 shows that electrolyte flow through micropatterned lithium metal electrodes shifts ions towards the slots resulting in increased plating and stripping over time in the slot and inter-slot gap, respectively. Higher electrolyte velocity leads to an early start of stripping in the inter-slot gap. Large inter-slot gaps and large electrode thickness reduce dendrite growth in inter-slot gap and stored charge density. Low slot widths lead to increased stored charge density and dendrite free inter-slot gaps and increased chances

of pore closure. For, the relatively large inter-electrode gap of 1 mm used in this study, slot widths lower than about 0.1 mm are not advisable. A slot width of 0.1 mm, electrode thickness of 10 μm, electrolyte inlet velocity of 200 nm/s, and an inter-slot gap of 1 mm ensures a relatively high stored charge density of 206 C/g and non-dendritic inter-slot gap within the first 1000 s of charging time.

Chapter 4 shows that creeping electrolyte flow parallel to the lithium metal electrode can reduce dendrite growth. Dendrites will grow at a slower rate and be flatter, so they will be less likely to penetrate the separator or fracture the SEI. Parallel flows must be several orders of magnitude higher than normal flows for similar reduction in instability. It is also not possible to completely stabilize electrodeposition with creeping flow parallel to the lithium metal electrode. For the same average flow rate, Poiseuille flow can be upto two times more stabilizing than Couette flow.

A small amount of electrolyte flow towards the metal electrode of a LMB during charging can produce remarkable results. As discussed in chapter 2, electrostatic potential decreases and dendrites disappear, making LMBs amenable to fast charging and safe operation. Chapter 5 shows for the first time that flow reduces SEI layer formation and increases coulombic efficiency. The critical flow rate is a key parameter in the design of FEMBs. It is the lowest flow rate that suppresses dendrites. Tuning flow rates and electrolyte parameters such as rate constants can enable fast charging, safe, dendrite-free, long-lasting lithium metal batteries.

Chapter 6 shows that electrolyte flow towards the zinc metal anode can suppress dendrite growth. Above the critical flow rate, surface irregularities will dissolve rather than grow. Supercritical flow will also eliminate overlimiting conditions at the anode surface,

suppressing a second dendrite growth mechanism. Flow flattens and reverses the slope of electrolyte concentration distribution and enabling fast charging without exceeding voltage limits associated with side reactions such as electrolysis.

Bibliography

[1] Whittingham, M. S. (2012) "History, evolution, and future status of energy storage," *Proceedings of the IEEE*, **100**(Special Centennial Issue), pp. 1518–1534.

[2] Liu, G. and W. Lu (2017) "A model of concurrent lithium dendrite growth, SEI growth, SEI penetration and regrowth," *Journal of The Electrochemical Society*, **164**(9), pp. A1826–A1833.

[3] Chazalviel, J.-N. (1990) "Electrochemical aspects of the generation of ramified metallic electrodeposits," *Physical review A*, **42**(12), p. 7355.

[4] Nishikawa, K., T. Mori, T. Nishida, Y. Fukunaka, and M. Rosso (2011) "Li dendrite growth and Li+ ionic mass transfer phenomenon," *Journal of electroanalytical chemistry*, **661**(1), pp. 84–89.

[5] Sand, H. J. (1901) "III. On the concentration at the electrodes in a solution, with special reference to the liberation of hydrogen by electrolysis of a mixture of copper sulphate and sulphuric acid," *The London, Edinburgh, and Dublin Philosophical Magazine and Journal of Science*, **1**(1), pp. 45–79.

[6] Brissot, C., M. Rosso, J.-N. Chazalviel, P. Baudry, and S. Lascaud (1998) "In situ study of dendritic growth inlithium/PEO-salt/lithium cells," *Electrochimica acta*, **43**(10-11), pp. 1569–1574.

[7] Kushima, A., K. P. So, C. Su, P. Bai, N. Kuriyama, T. Maebashi, Y. Fujiwara, M. Z. Bazant, and J. Li (2017) "Liquid cell transmission electron microscopy observation of lithium metal growth and dissolution: Root growth, dead lithium and lithium flotsams," *Nano Energy*, **32**, pp. 271–279.

[8] Jana, A., S. I. Woo, K. Vikrant, and R. E. García (2019) "Electrochemomechanics of lithium dendrite growth," *Energy & Environmental Science*, **12**(12), pp. 3595–3607.

[9] Mistry, A., C. Fear, R. Carter, C. T. Love, and P. P. Mukherjee (2018) "Electrolyte confinement alters lithium electrodeposition," *ACS Energy Letters*, **4**(1), pp. 156–162.

[10] Wood, K. N., E. Kazyak, A. F. Chadwick, K.-H. Chen, J.-G. Zhang, K. Thornton, and N. P. Dasgupta (2016) "Dendrites and pits: Untangling the complex behavior of lithium metal anodes through operando video microscopy," *ACS central science*, **2**(11), pp. 790–801.

[11] Ely, D. R. and R. E. García (2013) "Heterogeneous nucleation and growth of lithium electrodeposits on negative electrodes," *Journal of The Electrochemical Society*, **160**(4), pp. A662–A668.

[12] Akolkar, R. (2013) "Mathematical model of the dendritic growth during lithium electrodeposition," *Journal of Power Sources*, **232**, pp. 23–28.

[13] Yan, H., Y. Bie, X. Cui, G. Xiong, and L. Chen (2018) "A computational investigation of thermal effect on lithium dendrite growth," *Energy Conversion and Management*, **161**, pp. 193–204.

[14] Akolkar, R. (2014) "Modeling dendrite growth during lithium electrodeposition at sub-ambient temperature," *Journal of Power Sources*, **246**, pp. 84–89.

[15] Sundström, L.-G. and F. H. Bark (1995) "On morphological instability during electrodeposition with a stagnant binary electrolyte," *Electrochimica acta*, **40**(5), pp. 599–614.

[16] Tikekar, M. D., L. A. Archer, and D. L. Koch (2014) "Stability analysis of electrodeposition across a structured electrolyte with immobilized anions," *Journal of The Electrochemical Society*, **161**(6), pp. A847–A855.

[17] Khoo, E., H. Zhao, and M. Z. Bazant (2019) "Linear stability analysis of transient electrodeposition in charged porous media: suppression of dendritic growth by surface conduction," *Journal of The Electrochemical Society*, **166**(10), pp. A2280–A2299.

[18] Elezgaray, J., C. Léger, and F. Argoul (1998) "Linear stability analysis of unsteady galvanostatic electrodeposition in the two-dimensional diffusion-limited regime," *Journal of the Electrochemical Society*, **145**(6), p. 2016.

[19] Gireaud, L., S. Grugeon, S. Laruelle, B. Yrieix, and J.-M. Tarascon (2006) "Lithium metal stripping/plating mechanisms studies: A metallurgical approach," *Electrochemistry communications*, **8**(10), pp. 1639–1649.

[20] Yang, H., E. O. Fey, B. D. Trimm, N. Dimitrov, and M. S. Whittingham (2014) "Effects of pulse plating on lithium electrodeposition, morphology and cycling efficiency," *Journal of Power Sources*, **272**, pp. 900–908.

[21] Mayers, M. Z., J. W. Kaminski, and T. F. Miller III (2012) "Suppression of dendrite formation via pulse charging in rechargeable lithium metal batteries," *The Journal of Physical Chemistry C*, **116**(50), pp. 26214–26221.

[22] Aryanfar, A., D. Brooks, B. V. Merinov, W. A. Goddard III, A. J. Colussi, and M. R. Hoffmann (2014) "Dynamics of lithium dendrite growth and inhibition: Pulse charging experiments and Monte Carlo calculations," *The journal of physical chemistry letters*, **5**(10), pp. 1721–1726.

[23] Maraschky, A. and R. Akolkar (2018) "Mechanism Explaining the Onset Time of Dendritic Lithium Electrodeposition via Considerations of the Li+ Transport within the Solid Electrolyte Interphase," *Journal of The Electrochemical Society*, **165**(14), p. D696.

[24] Chen, K.-H., K. N. Wood, E. Kazyak, W. S. LePage, A. L. Davis, A. J. Sanchez, and N. P. Dasgupta (2017) "Dead lithium: mass transport effects on voltage, capacity, and failure of lithium metal anodes," *Journal of Materials Chemistry A*, **5**(23), pp. 11671–11681.

[25] Maraschky, A. and R. Akolkar (2020) "Temperature Dependence of Dendritic Lithium Electrodeposition: A Mechanistic Study of the Role of Transport Limitations within the SEI," *Journal of The Electrochemical Society*, **167**(6), p. 062503.

[26] Li, G., Y. Gao, X. He, Q. Huang, S. Chen, S. H. Kim, and D. Wang (2017) "Organosulfide-plasticized solid-electrolyte interphase layer enables stable lithium metal anodes for long-cycle lithium-sulfur batteries," *Nature communications*, **8**(1), p. 850.

[27] Zheng, J., M. H. Engelhard, D. Mei, S. Jiao, B. J. Polzin, J.-G. Zhang, and W. Xu (2017) "Electrolyte additive enabled fast charging and stable cycling lithium metal batteries," *Nature Energy*, **2**(3), p. 17012.

[28] Qian, J., W. A. Henderson, W. Xu, P. Bhattacharya, M. Engelhard, O. Borodin, and J.-G. Zhang (2015) "High rate and stable cycling of lithium metal anode," *Nature communications*, **6**, p. 6362.

[29] Suo, L., Y.-S. Hu, H. Li, M. Armand, and L. Chen (2013) "A new class of solvent-in-salt electrolyte for high-energy rechargeable metallic lithium batteries," *Nature communications*, **4**, p. 1481.

[30] Liu, Y., D. Lin, P. Y. Yuen, K. Liu, J. Xie, R. H. Dauskardt, and Y. Cui (2017) "An artificial solid electrolyte interphase with high Li-ion conductivity, mechanical strength, and flexibility for stable lithium metal anodes," *Advanced Materials*, **29**(10), p. 1605531.

[31] Zhu, B., Y. Jin, X. Hu, Q. Zheng, S. Zhang, Q. Wang, and J. Zhu (2017) "Poly (dimethylsiloxane) Thin Film as a Stable Interfacial Layer for High-Performance Lithium-Metal Battery Anodes," *Advanced Materials*, **29**(2), p. 1603755.

[32] Kim, P. J., K. Kim, and V. G. Pol (2018) "Uniform metal-ion flux through interface-modified membrane for highly stable metal batteries," *Electrochimica Acta*, **283**, pp. 517–527.

[33] Cheng, X.-B., T.-Z. Hou, R. Zhang, H.-J. Peng, C.-Z. Zhao, J.-Q. Huang, and Q. Zhang (2016) "Dendrite-Free Lithium Deposition Induced by Uniformly Distributed Lithium Ions for Efficient Lithium Metal Batteries," *Advanced Materials*, **28**(15), pp. 2888–2895.

[34] Fan, L., H. L. Zhuang, W. Zhang, Y. Fu, Z. Liao, and Y. Lu (2018) "Stable Lithium Electrodeposition at Ultra-High Current Densities Enabled by 3D PMF/Li Composite Anode," *Advanced Energy Materials*, **8**(15), p. 1703360.

[35] Zhang, C., S. Liu, G. Li, C. Zhang, X. Liu, and J. Luo (2018) "Incorporating Ionic Paths into 3D Conducting Scaffolds for High Volumetric and Areal Capacity, High Rate Lithium-Metal Anodes," *Advanced Materials*, **30**(33), p. 1801328.

[36] Li, N., Q. Ye, K. Zhang, H. Yan, C. Shen, B. Wei, and K. Xie (2019) "Normalization Li growth from nucleation stage for dendrite-free Li metal anodes," *Angewandte Chemie International Edition*.

[37] Wang, C., A. Wang, L. Ren, X. Guan, D. Wang, A. Dong, C. Zhang, G. Li, and J. Luo (2019) "Controlling Li Ion Flux through Materials Innovation for Dendrite-Free Lithium Metal Anodes," *Advanced Functional Materials*.

[38] Bai, P., J. Guo, M. Wang, A. Kushima, L. Su, J. Li, F. R. Brushett, and M. Z. Bazant (2018) "Interactions between lithium growths and nanoporous ceramic separators," *Joule*, **2**(11), pp. 2434–2449.

[39] Bai, P., J. Li, F. R. Brushett, and M. Z. Bazant (2016) "Transition of lithium growth mechanisms in liquid electrolytes," *Energy & Environmental Science*, **9**(10), pp. 3221–3229.

[40] Rehnlund, D., C. Ihrfors, J. Maibach, and L. Nyholm (2018) "Dendrite-free lithium electrode cycling via controlled nucleation in low LiPF6 concentration electrolytes," *Materials Today*, **21**(10), pp. 1010–1018.

[41] Yang, X., Z. Wen, X. Zhu, and S. Huang (2005) "Electrodeposition of lithium film under dynamic conditions and its application in all-solid-state rechargeable lithium battery," *Solid State Ionics*, **176**(11-12), pp. 1051–1055.

[42] Wang, A., Q. Deng, L. Deng, X. Guan, and J. Luo (2019) "Eliminating Tip Dendrite Growth by Lorentz Force for Stable Lithium Metal Anodes," *Advanced Functional Materials*, p. 1902630.

[43] Li, G., Z. Liu, Q. Huang, Y. Gao, M. Regula, D. Wang, L.-Q. Chen, and D. Wang (2018) "Stable metal battery anodes enabled by polyethylenimine sponge hosts by way of electrokinetic effects," *Nature Energy*, **3**(12), p. 1076.

[44] Tan, J. and E. M. Ryan (2016) "Computational study of electro-convection effects on dendrite growth in batteries," *Journal of Power Sources*, **323**, pp. 67–77.

[45] Peled, E. (1979) "The electrochemical behavior of alkali and alkaline earth metals in nonaqueous battery systemsthe solid electrolyte interphase model," *Journal of The Electrochemical Society*, **126**(12), p. 2047.

[46] Shi, F., A. Pei, D. T. Boyle, J. Xie, X. Yu, X. Zhang, and Y. Cui (2018) "Lithium metal stripping beneath the solid electrolyte interphase," *Proceedings of the National Academy of Sciences*, **115**(34), pp. 8529–8534.

[47] Lu, D., Y. Shao, T. Lozano, W. D. Bennett, G. L. Graff, B. Polzin, J. Zhang, M. H. Engelhard, N. T. Saenz, W. A. Henderson, et al. (2015) "Failure mechanism for fast-charged lithium metal batteries with liquid electrolytes," *Advanced Energy Materials*, **5**(3), p. 1400993.

[48] Aurbach, D. (2000) "Review of selected electrode–solution interactions which determine the performance of Li and Li ion batteries," *Journal of Power Sources*, **89**(2), pp. 206–218.

[49] Jiang, Y., B. Wang, P. Liu, B. Wang, Y. Zhou, D. Wang, H. Liu, and S. Dou (2020) "Modified solid-electrolyte interphase toward stable Li metal anode," *Nano Energy*, p. 105308.

[50] Broussely, M., S. Herreyre, P. Biensan, P. Kasztejna, K. Nechev, and R. Staniewicz (2001) "Aging mechanism in Li ion cells and calendar life predictions," *Journal of Power Sources*, **97**, pp. 13–21.

[51] Ploehn, H. J., P. Ramadass, and R. E. White (2004) "Solvent diffusion model for aging of lithium-ion battery cells," *Journal of The Electrochemical Society*, **151**(3), pp. A456–A462.

[52] Christensen, J. and J. Newman (2004) "A mathematical model for the lithium-ion negative electrode solid electrolyte interphase," *Journal of The Electrochemical Society*, **151**(11), pp. A1977–A1988.

[53] Pinson, M. B. and M. Z. Bazant (2012) "Theory of SEI formation in rechargeable batteries: capacity fade, accelerated aging and lifetime prediction," *Journal of the Electrochemical Society*, **160**(2), p. A243.

[54] Single, F., A. Latz, and B. Horstmann (2018) "Identifying the mechanism of continued growth of the solid-electrolyte interphase," *arXiv preprint arXiv:1812.03841*.

[55] Tanim, T. R. and C. D. Rahn (2015) "Aging formula for lithium ion batteries with solid electrolyte interphase layer growth," *Journal of Power Sources*, **294**, pp. 239–247.

[56] Attia, P. M., S. Das, S. J. Harris, M. Z. Bazant, and W. C. Chueh (2019) "Electrochemical kinetics of SEI growth on carbon black: part I. Experiments," *Journal of The Electrochemical Society*, **166**(4), pp. E97–E106.

[57] Das, S., P. M. Attia, W. C. Chueh, and M. Z. Bazant (2019) "Electrochemical kinetics of SEI growth on carbon black: part II. Modeling," *Journal of The Electrochemical Society*, **166**(4), pp. E107–E118.

[58] Kim, S.-P., A. C. Van Duin, and V. B. Shenoy (2011) "Effect of electrolytes on the structure and evolution of the solid electrolyte interphase (SEI) in Li-ion batteries: A molecular dynamics study," *Journal of Power Sources*, **196**(20), pp. 8590–8597.

[59] Bertolini, S. and P. B. Balbuena (2018) "Buildup of the solid electrolyte interphase on lithium-metal anodes: reactive molecular dynamics study," *The Journal of Physical Chemistry C*, **122**(20), pp. 10783–10791.

[60] Michan, A. L., B. S. Parimalam, M. Leskes, R. N. Kerber, T. Yoon, C. P. Grey, and B. L. Lucht (2016) "Fluoroethylene carbonate and vinylene carbonate reduction: Understanding lithium-ion battery electrolyte additives and solid electrolyte interphase formation," *Chemistry of Materials*, **28**(22), pp. 8149–8159.

[61] Matsuda, Y. (1993) "Behavior of lithium/electrolyte interface in organic solutions," *Journal of Power Sources*, **43**(1-3), pp. 1–7.

[62] Aurbach, D. and A. Zaban (1993) "Impedance spectroscopy of lithium electrodes: Part 1. General behavior in propylene carbonate solutions and the correlation to surface chemistry and cycling efficiency," *Journal of Electroanalytical Chemistry*, **348**(1-2), pp. 155–179.

[63] Ishikawa, M., Y. Tasaka, N. Yoshimoto, and M. Morita (2001) "Optimization of physicochemical characteristics of a lithium anode interface for high-efficiency cycling: an effect of electrolyte temperature," *Journal of Power Sources*, **97**, pp. 262–264.

[64] Dolle, M., S. Grugeon, B. Beaudoin, L. Dupont, and J. Tarascon (2001) "In situ TEM study of the interface carbon/electrolyte," *Journal of power sources*, **97**, pp. 104–106.

[65] Lee, Y. M., J. E. Seo, Y.-G. Lee, S. H. Lee, K. Y. Cho, and J.-K. Park (2007) "Effects of triacetoxyvinylsilane as SEI layer additive on electrochemical performance of lithium metal secondary battery," *Electrochemical and Solid State Letters*, **10**(9), p. A216.

[66] Heine, J., P. Hilbig, X. Qi, P. Niehoff, M. Winter, and P. Bieker (2015) "Fluoroethylene carbonate as electrolyte additive in tetraethylene glycol dimethyl

ether based electrolytes for application in lithium ion and lithium metal batteries," *Journal of the Electrochemical Society*, **162**(6), p. A1094.

[67] Zhao, C.-Z., Q. Zhao, X. Liu, J. Zheng, S. Stalin, Q. Zhang, and L. A. Archer (2020) "Rechargeable Lithium Metal Batteries with an In-Built Solid-State Polymer Electrolyte and a High Voltage/Loading Ni-Rich Layered Cathode," *Advanced Materials*, **32**(12), p. 1905629.

[68] Li, N.-W., Y.-X. Yin, C.-P. Yang, and Y.-G. Guo (2016) "An artificial solid electrolyte interphase layer for stable lithium metal anodes," *Advanced Materials*, **28**(9), pp. 1853–1858.

[69] Pathak, R., K. Chen, A. Gurung, K. M. Reza, B. Bahrami, J. Pokharel, A. Baniya, W. He, F. Wu, Y. Zhou, et al. (2020) "Fluorinated hybrid solid-electrolyte-interphase for dendrite-free lithium deposition," *Nature Communications*, **11**(1), pp. 1–10.

[70] Wang, F., G. Chen, N. Zhang, X. Liu, and R. Ma (2019) "Engineering of carbon and other protective coating layers for stabilizing silicon anode materials," *Carbon Energy*, **1**(2), pp. 219–245.

[71] Gao, Y., Z. Yan, J. L. Gray, X. He, D. Wang, T. Chen, Q. Huang, Y. C. Li, H. Wang, S. H. Kim, et al. (2019) "Polymer–inorganic solid–electrolyte interphase for stable lithium metal batteries under lean electrolyte conditions," *Nature Materials*, **18**(4), pp. 384–389.

[72] Ju, Z., J. Nai, Y. Wang, T. Liu, J. Zheng, H. Yuan, O. Sheng, C. Jin, W. Zhang, Z. Jin, et al. (2020) "Biomacromolecules enabled dendrite-free lithium metal battery and its origin revealed by cryo-electron microscopy," *Nature Communications*, **11**(1), pp. 1–10.

[73] Fan, X., L. Chen, X. Ji, T. Deng, S. Hou, J. Chen, J. Zheng, F. Wang, J. Jiang, K. Xu, et al. (2018) "Highly fluorinated interphases enable high-voltage Li-metal batteries," *Chem*, **4**(1), pp. 174–185.

[74] Wang, M., L. Huai, G. Hu, S. Yang, F. Ren, S. Wang, Z. Zhang, Z. Chen, Z. Peng, C. Shen, et al. (2018) "Effect of LiFSI concentrations to form thickness-and modulus-controlled SEI layers on lithium metal anodes," *The Journal of Physical Chemistry C*, **122**(18), pp. 9825–9834.

[75] Cui, C., C. Yang, N. Eidson, J. Chen, F. Han, L. Chen, C. Luo, P.-F. Wang, X. Fan, and C. Wang (2020) "A Highly Reversible, Dendrite-Free Lithium Metal Anode Enabled by a Lithium-Fluoride-Enriched Interphase," *Advanced Materials*, **32**(12), p. 1906427.

[76] Liu, S., X. Ji, J. Yue, S. Hou, P. Wang, C. Cui, J. Chen, B. Shao, J. Li, F. Han, et al. (2020) "High interfacial-energy interphase promoting safe lithium

metal batteries," *Journal of the American Chemical Society*, **142**(5), pp. 2438–2447.

[77] Huo, H., X. Li, Y. Chen, J. Liang, S. Deng, X. Gao, K. Doyle-Davis, R. Li, X. Guo, Y. Shen, et al. (2020) "Bifunctional composite separator with a solid-state-battery strategy for dendrite-free lithium metal batteries," *Energy Storage Materials*, **29**, pp. 361–366.

[78] Liang, J., Q. Chen, X. Liao, P. Yao, B. Zhu, G. Lv, X. Wang, X. Chen, and J. Zhu (2020) "A Nano-shield Design for Separators to Resist Dendrite Formation in Lithium-Metal Batteries," *Angewandte Chemie International Edition*, **59**(16), pp. 6561–6566.

[79] Ma, L., M. S. Kim, and L. A. Archer (2017) "Stable artificial solid electrolyte interphases for lithium batteries," *Chemistry of Materials*, **29**(10), pp. 4181–4189.

[80] Huang, A., H. Liu, O. Manor, P. Liu, and J. Friend (2020) "Enabling Rapid Charging Lithium Metal Batteries via Surface Acoustic Wave-Driven Electrolyte Flow," *Advanced Materials*, p. 1907516.

[81] Chalamala, B. (2018) *Emerging Energy Storage Technologies Safety and Standards.*, *Tech. rep.*, Sandia National Lab.(SNL-NM), Albuquerque, NM (United States).

[82] Yadav, G. G., X. Wei, J. Huang, J. W. Gallaway, D. E. Turney, M. Nyce, J. Secor, and S. Banerjee (2017) "A conversion-based highly energy dense Cu 2+ intercalated Bi-birnessite/Zn alkaline battery," *Journal of Materials Chemistry A*, **5**(30), pp. 15845–15854.

[83] Karpinski, A., B. Makovetski, S. Russell, J. Serenyi, and D. Williams (1999) "Silver–zinc: status of technology and applications," *Journal of Power Sources*, **80**(1-2), pp. 53–60.

[84] Zheng, J., Q. Zhao, T. Tang, J. Yin, C. D. Quilty, G. D. Renderos, X. Liu, Y. Deng, L. Wang, D. C. Bock, et al. (2019) "Reversible epitaxial electrodeposition of metals in battery anodes," *Science*, **366**(6465), pp. 645–648.

[85] Higashi, S., S. W. Lee, J. S. Lee, K. Takechi, and Y. Cui (2016) "Avoiding short circuits from zinc metal dendrites in anode by backside-plating configuration," *Nature communications*, **7**(1), pp. 1–6.

[86] Liu, K., Y. Liu, D. Lin, A. Pei, and Y. Cui (2018) "Materials for lithium-ion battery safety," *Science advances*, **4**(6), p. eaas9820.

[87] Zheng, J. and L. A. Archer (2021) "Controlling electrochemical growth of metallic zinc electrodes: Toward affordable rechargeable energy storage systems," *Science Advances*, **7**(2), p. eabe0219.

[88] Zheng, J., J. Yin, D. Zhang, G. Li, T. Tang, Q. Zhao, X. Liu, A. Warren, Y. Deng, S. Jin, C. D. Rahn, and L. A. Archer "Spontaneous and field induced crystallographic reorientation of metal electrodeposits at battery anodes," .

[89] Langer, J. S. (1980) "Instabilities and pattern formation in crystal growth," *Reviews of modern physics*, **52**(1), p. 1.

[90] Léger, C., J. Elezgaray, and F. Argoul (1997) "Experimental demonstration of diffusion-limited dynamics in electrodeposition," *Physical review letters*, **78**(26), p. 5010.

[91] Yufit, V., F. Tariq, D. S. Eastwood, M. Biton, B. Wu, P. D. Lee, and N. P. Brandon (2019) "Operando visualization and multi-scale tomography studies of dendrite formation and dissolution in zinc batteries," *Joule*, **3**(2), pp. 485–502.

[92] López, C. M. and K.-S. Choi (2006) "Electrochemical synthesis of dendritic zinc films composed of systematically varying motif crystals," *Langmuir*, **22**(25), pp. 10625–10629.

[93] Sawada, Y., A. Dougherty, and J. P. Gollub (1986) "Dendritic and fractal patterns in electrolytic metal deposits," *Physical review letters*, **56**(12), p. 1260.

[94] Matsushita, M., M. Sano, Y. Hayakawa, H. Honjo, and Y. Sawada (1984) "Fractal structures of zinc metal leaves grown by electrodeposition," *Physical review letters*, **53**(3), p. 286.

[95] Argoul, F., A. Arneodo, G. Grasseau, and H. L. Swinney (1988) "Self-similarity of diffusion-limited aggregates and electrodeposition clusters," *Physical review letters*, **61**(22), p. 2558.

[96] Elezgaray, J., C. Léger, and F. Argoul (2000) "Dense branching morphology in electrodeposition experiments: Characterization and mean-field modeling," *Physical review letters*, **84**(14), p. 3129.

[97] Yang, Q., G. Liang, Y. Guo, Z. Liu, B. Yan, D. Wang, Z. Huang, X. Li, J. Fan, and C. Zhi (2019) "Do zinc dendrites exist in neutral zinc batteries: a developed electrohealing strategy to in situ rescue in-service batteries," *Advanced materials*, **31**(43), p. 1903778.

[98] Zuo, Y., K. Wang, P. Pei, M. Wei, X. Liu, Y. Xiao, and P. Zhang (2021) "Zinc dendrite growth and inhibition strategies," *Materials Today Energy*, p. 100692.

[99] Kim, H.-I. and H.-C. Shin (2015) "SnO additive for dendritic growth suppression of electrolytic zinc," *Journal of Alloys and Compounds*, **645**, pp. 7–10.

[100] Shimizu, M., K. Hirahara, and S. Arai (2019) "Morphology control of zinc electrodeposition by surfactant addition for alkaline-based rechargeable batteries," *Physical Chemistry Chemical Physics*, **21**(13), pp. 7045–7052.

[101] Xu, W., K. Zhao, W. Huo, Y. Wang, G. Yao, X. Gu, H. Cheng, L. Mai, C. Hu, and X. Wang (2019) "Diethyl ether as self-healing electrolyte additive enabled long-life rechargeable aqueous zinc ion batteries," *Nano Energy*, **62**, pp. 275–281.

[102] Zhao, S., L. C. Player, S. A. Bartlett, A. F. Masters, and T. Maschmeyer (2019) "The Influence of Pyridinium-Based Additives on Zinc Electrodeposition in Aqueous Solution," *Journal of The Electrochemical Society*, **166**(6), p. D192.

[103] Bae, S., J. Lee, and D. S. Kim (2019) "The effect of Cr3+-Functionalized additive in zinc-bromine flow battery," *Journal of Power Sources*, **413**, pp. 167–173.

[104] Wang, K., P. Pei, Z. Ma, H. Xu, P. Li, and X. Wang (2014) "Morphology control of zinc regeneration for zinc–air fuel cell and battery," *Journal of Power Sources*, **271**, pp. 65–75.

[105] Yang, X., S. Liu, J. Tang, G. Chang, Y. Fu, W. Jin, X. Ji, and J. Hu (2019) "Effective inhibition of zinc dendrites during electrodeposition using thiourea derivatives as additives," *Journal of Materials Science*, **54**(4), pp. 3536–3546.

[106] Chang, G., S. Liu, Y. Fu, X. Hao, W. Jin, X. Ji, and J. Hu (2019) "Inhibition role of trace metal ion additives on zinc dendrites during plating and striping processes," *Advanced Materials Interfaces*, **6**(23), p. 1901358.

[107] Yu, W., W. Shang, X. Xiao, P. Tan, B. Chen, Z. Wu, H. Xu, and M. Ni (2020) "Achieving a stable zinc electrode with ultralong cycle life by implementing a flowing electrolyte," *Journal of Power Sources*, **453**, p. 227856.

[108] Crowther, O. and A. C. West (2008) "Effect of electrolyte composition on lithium dendrite growth," *Journal of The Electrochemical Society*, **155**(11), pp. A806–A811.

[109] Wlasenko, A., F. Soltani, D. Zakopcan, D. Sinton, and G. Steeves (2010) "Diffusion-limited and advection-driven electrodeposition in a microfluidic channel," *Physical Review E*, **81**(2), p. 021601.

[110] Electrodeposition Module User's Guide, pp. 150-151. COMSOL Multiphysicső v. 5.4. COMSOL AB, Stockholm, Sweden. 2018.

[111] CFD Module User's Guide, pp. 60. COMSOL Multiphysicső v. 5.4. COMSOL AB, Stockholm, Sweden. 2018.

[112] COMSOL Multiphysics® v. 5.4, www.comsol.com, COMSOL AB, Stockholm, Sweden.

[113] Https://www.sigmaaldrich.com/catalog/product/aldrich /746711?lang=enregion=US.

[114] Dougassa, Y. R., J. Jacquemin, L. El Ouatani, C. Tessier, and M. Anouti (2014) "Viscosity and carbon dioxide solubility for LiPF6, LiTFSI, and LiFAP in alkyl carbonates: lithium salt nature and concentration effect," *The Journal of Physical Chemistry B*, **118**(14), pp. 3973–3980.

[115] Lee, S.-I., U.-H. Jung, Y.-S. Kim, M.-H. Kim, D.-J. Ahn, and H.-S. Chun (2002) "A study of electrochemical kinetics of lithium ion in organic electrolytes," *Korean Journal of Chemical Engineering*, **19**(4), pp. 638–644.

[116] Https://en.wikipedia.org/wiki/Electron-beam_lithography.

[117] Https://education.jlab.org/itselemental/ele003.html.

[118] Zaltzman, B. and I. Rubinstein (2007) "Electro-osmotic slip and electroconvective instability," *Journal of Fluid Mechanics*, **579**, p. 173.

[119] Single, F., B. Horstmann, and A. Latz (2017) "Revealing SEI morphology: in-depth analysis of a modeling approach," *Journal of The Electrochemical Society*, **164**(11), pp. E3132–E3145.

[120] Harris, S. J. and P. Lu (2013) "Effects of Inhomogeneities Nanoscale to Mesoscale on the Durability of Li-Ion Batteries," *The Journal of Physical Chemistry C*, **117**(13), pp. 6481–6492.

[121] Parekh, M. N., C. D. Rahn, and L. A. Archer (2020) "Controlling dendrite growth in lithium metal batteries through forced advection," *Journal of Power Sources*, **452**, p. 227760.

[122] Iverson, B. D. and S. V. Garimella (2008) "Recent advances in microscale pumping technologies: a review and evaluation," *Microfluidics and nanofluidics*, **5**(2), pp. 145–174.

[123] Park, J., J. Jeong, Y. Lee, M. Oh, M.-H. Ryou, and Y. M. Lee (2016) "Micro-patterned lithium metal anodes with suppressed dendrite formation for post lithium-ion batteries," *Advanced Materials Interfaces*, **3**(11), p. 1600140.

[124] Ryou, M.-H., Y. M. Lee, Y. Lee, M. Winter, and P. Bieker (2015) "Mechanical surface modification of lithium metal: towards improved Li metal anode performance by directed Li plating," *Advanced Functional Materials*, **25**(6), pp. 834–841.

[125] Wang, S.-H., Y.-X. Yin, T.-T. Zuo, W. Dong, J.-Y. Li, J.-L. Shi, C.-H. Zhang, N.-W. Li, C.-J. Li, and Y.-G. Guo (2017) "Stable Li metal anodes via regulating lithium plating/stripping in vertically aligned microchannels," *Advanced Materials*, **29**(40), p. 1703729.

[126] Harned, H. S. and R. M. Hudson (1951) "The diffusion coefficient of zinc sulfate in dilute aqueous solution at 25ř," *Journal of the American Chemical Society*, **73**(8), pp. 3781–3783.

[127] de Carvalho Izidoro, J., D. A. Fungaro, and S. B. Wang (2012) "Zeolite synthesis from Brazilian coal fly ash for removal of Zn2+ and Cd2+ from water," in *Advanced Materials Research*, vol. 356, Trans Tech Publ, pp. 1900–1908.

[128] Tanganov, B. (2013) "About sizes of the hydrated salt ions–the components of sea water," *European Journal of Natural History*, (1), pp. 36–37.

[129] Maitland, A. and G. Chadwick (1969) "The cleavage surface energy of zinc," *Philosophical Magazine*, **19**(160), pp. 645–651.

[130] Http://www.knowledgedoor.com/2/elements_handbook/molar_volume.html.

Vita

Mihir Parekh

Education

- **The Pennsylvania State University** (Aug '18 – Jul '21) CGPA:4.0/4.0
  Ph.D. in Mechanical Engineering and minor in Computational Materials Science
- **Indian Institute of Technology Bombay**(Jul '13 – Jun '18) CGPA:9.37/10
  B. Tech and M. Tech in Energy Engineering and minor in Electrical Engineering

Publications

- **Parekh MN**, Rahn CD, Archer LA. Controlling dendrite growth in lithium metal batteries through forced advection. Journal of Power Sources. 2020 Mar 15;452:227760.
- **Parekh M**, Rahn C. Dendrite Suppression and Energy Density in Metal Batteries With Electrolyte Flow Through Perforated Electrodes. In ASME International Mechanical Engineering Congress and Exposition 2020 Nov 16 (Vol. 84560, p. V008T08A018). American Society of Mechanical Engineers.
- **Parekh MN**, Rahn CD. Reducing Dendrite Growth in Lithium Metal Batteries by Creeping Poiseuille and Couette Flows. Journal of the Electrochemical Society. 2020 Dec 10;167(16):160525.
- **Parekh MN**, and Christopher D. Rahn."Solid electrolyte interphase growth in lithium metal cells with normal electrolyte flow"*POWER 2022-ASME Power conference* (**Under preparation**)
- **Parekh M** and Rahn C. "Flowing electrolyte metal batteries." *239th ECS meeting with 18th International Meeting on Chemical Sensors (IMCS) (May 30-June 3, 2021)* (**Conference Presentation**)
- **Parekh MN** and Rahn CD. Effect of supercapacitor size, starting state of charge, and power management schemes on a system of wearable energy harvesters. (**Under preparation**)

Speaking Invitation

- Battery Safety Summit, Alexandria, Virginia, USA (Oct '20) (*canceled due to COVID-19*)
- PlugVolt LLC, Webinar (Mar '21)

Professional Experience

- Continuum Wind Energy Pvt. Ltd.